Article

Synthesis and Nonlinear Optical Behavior of Thermally Stable Chromophores Based on 9,9-Dimethyl-9H-fluoren-2-amine: Improving Intrinsic Hyperpolarizability through Modulation of "Push−Pull"

Shivani, Akriti Mishra, Paramjit Kaur,* and Kamaljit Singh*

Cite This: *ACS Omega* 2022, 7, 39045−39060

Read Online

ACCESS | Metrics & More | Article Recommendations | SI Supporting Information

ABSTRACT: Improvement in the first hyperpolarizability (β_{HRS}) as well as intrinsic hyperpolarizability (β^{int}) of chromophores based on 9,9-dimethyl-9H-fluoren-2-amine through modulation of the conjugation pathway is described. A series of six novel chromophores with "linear" conjugation showed significant enhancement of β_{HRS} as well as β^{int} compared to the counterparts lacking a "linear" conjugation but having an identical combination of donor, acceptor, and the intervening π-conjugated linker. The hyperpolarizability (β_{HRS} as well as β^{int}) values of the new series measured using hyper-Rayleigh scattering exceeded the apparent limit set by the latter set of fluorene-based chromophores. The experimental results are analyzed and interpreted in the context of linear optical properties, single-crystal X-ray analysis, electrochemistry, etc. and corroborated by theoretical studies. We find that modulation of the "push−pull" of the conjugation pathway in these donor−acceptor chromophores compares favourably with the corresponding changes in the optical gaps, transition dipole moments, and dipole moment difference between the ground and excited states.
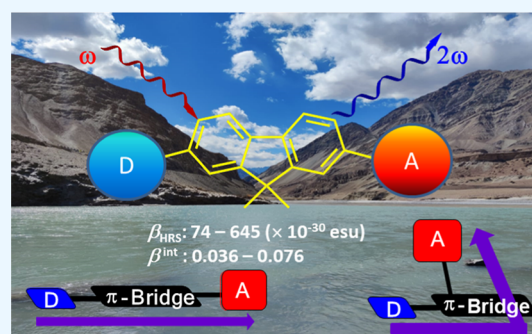
1. INTRODUCTION

The demand for nonlinear optical (NLO) materials with superior properties has created enormous interest among the scientific community due to their application in optical switching,[1−3] sensor protection,[4] light modulation,[5,6] memory storage devices,[7] information processing,[8,9] telecommunications,[10] and similar applications. It has sensitized investigations in the design of new chemical entities having ultrafast response (short response time) as well as high first (quadratic) hyperpolarizability (β, second-order nonlinear polarizability).[11,12] One of the strategies for molecular engineering to design the small molecular materials is to append the electron-rich and electron-deficient groups at the two extremes of a π-conjugated linker unit to produce 1D dipolar donor−π−acceptor (D−π−A)-type architectures.[13,14] Optimization of molecular NLO response of such dyads is important as these constitute fundamental building blocks for the bulk materials with bulk nonlinear susceptibility.[15] For enhancing the molecular first hyperpolarizability, noncentrosymmetry[16,17] of the compounds is an essential prerequisite. However, most "push−pull"-type D−π−A chromophores are inherently centrosymmetric unless an element of dissymmetry is incorporated.[16,18] Alternatively, when incorporated in non-centrosymmetric media, such chromophores show second-order nonlinear bulk susceptibility.[19] Thus, the centrosym-metric chromophores are also valuable NLO-phores, and it has led to the synthesis and understanding of the NLO behavior of several classes of centrosymmetric chromophores.[20] The structural features of such integrated dyads allow fine-tuning of the energies of the frontier molecular orbital (FMO) levels and the associated HOMO−LUMO gap, light absorption and emission abilities, intramolecular charge transfer (ICT), and intermolecular charge separation and recombination through the flexible structural adjustability by tuning of the length and path of the π-conjugation, which constitute important attributes of efficient NLO-phores. In this context, structure modification of several classes of molecular scaffolds and tuning of the π-conjugation by modulating its length and/or strength of donor and acceptor units have resulted in highly efficient NLO-phores.[21−23] One of the elements of π-conjugation that has rather scarcely been addressed is the understanding of the influence of the path (linear *vs* nonlinear, Figure 1) of π-conjugation[23,24] within the donor−π−acceptor
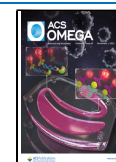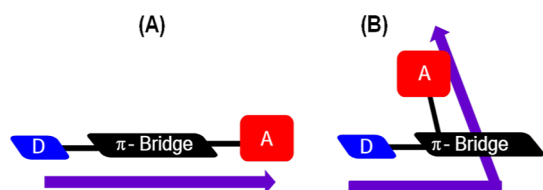
Figure 1. Linear (A) and nonlinear (B) pathways of π-conjugation in D−π−A dyads.

class of NLO materials for obtaining high β. There are, however, several reports[23,25,26] on the influence of appending groups of variable strength on the donor or acceptor moieties as well as changing the length of the π-conjugated bridge linking the donor and the acceptor.

In continuation of our interest in designing D−π−A dyads as small-molecule-based NLO materials, we herein demonstrate a direct comparison of the π-conjugation path (linear *vs* nonlinear) and dependence of nonlinear efficiency on a linear conjugation pathway. We have compared the first hyperpolarizability (β_{HRS}) as well as the intrinsic first hyperpolarizability (β^{int}) of the chromophores based on 9,9-dimethyl-9H-fluoren-2-amine, possessing a linear conjugation path with a "design-deficient" series of chromophores,[27] having similar molecular size, same number of conjugating electrons, and donor−acceptor groups attached at different positions on the fluorene unit, resulting in a "nonlinear" conjugation path. We report the synthesis, photophysical properties, electrochemistry, thermogravimetric studies, as well as NLO behavior of these compounds. Additionally, the single-crystal X-ray structures of two chromophores were determined for an unambiguous assignment of structures as well as to correlate the β_{HRS} with the solid-state structures. Further, we demonstrate unequivocal superiority of the NLO response of the current, "linear" molecular design over the design-deficient "nonlinear" chromophores[27] of the same chemical constitution.

2. RESULTS AND DISCUSSION

The design strategy and the structures of linearly conjugated D−π−A chromophores are shown in Figure 2. The chromophores are based on fluorene units, which are appended with a dimethylamino donor and different acceptors including dicyanovinyl, 2-(3-vinyl-5,5-dimethylcyclohex-2-en-1-ylidene)malononitrile, and cyanostilbene groups. The synthesis of chromophores **SS1**−**SS5** (Figure 2) started from a common precursor 2-(dimethylamino)-9,9-dimethyl-9H-fluorene-3-carbaldehyde **8** obtained through the route outlined in Scheme 1. Thus, nucleophilic substitution of the bromo group of 2-bromo-9,9-dimethyl-7-nitro-9H-fluorene **4** with CuCN yielded 9,9-dimethyl-7-nitro-9H-fluorene-2-carbonitrile **5** in high yield. Reduction of the nitro group of **5** using hydrazine furnished 7-amino-9,9-dimethyl-9H-fluorene-2-carbonitrile **6**, which upon reductive methylation using paraformaldehyde and sodium cyanoborohydride yielded the dimethyl derivative, 7-(dimethylamino)-9,9-dimethyl-9H-fluorene-2-carbonitrile **7**.

Finally, reduction of CN to CHO was achieved using diisobutylaluminium hydride (DIBAL) to obtain the intermediate 7-(dimethylamino)-9,9-dimethyl-9H-fluorene-2-carbaldehyde **8** in 69% yield. Knoevenagel condensation of **8** with different active methylene compounds malononitrile, 2-(3,5,5-trimethylcyclohex-2-en-1-ylidene)malononitrile [obtained through Knoevenagel condensation of 3,5,5-trimethylcyclohex-2-en-1-one (isophorone) and malononitrile], 2-(4-bromophenyl)acetonitrile, and 2-(4-nitrophenyl)acetonitrile using piperidine or KOH as a base yielded 2-((7-(dimethylamino)-9,9-dimethyl-9H-fluoren-2-yl)methylene)-malononitrile (**SS1**, 69%), (E)-2-(3-(2-(7-(dimethylamino)-9,9-dimethyl-9H-fluoren-2-yl)vinyl)-5,5-dimethylcyclohex-2-en-1-ylidene)malononitrile (**SS2**, 78%), (E)-2-(4-bromophenyl)-3-(7-(dimethylamino)-9,9-dimethyl-9H-fluoren-2-yl)-acrylonitrile (**SS3**, 80%), and (E)-3-(7-(dimethylamino)-9,9-dimethyl-9H-fluoren-2-yl)-2-(4-nitrophenyl)acrylonitrile (**SS4**,
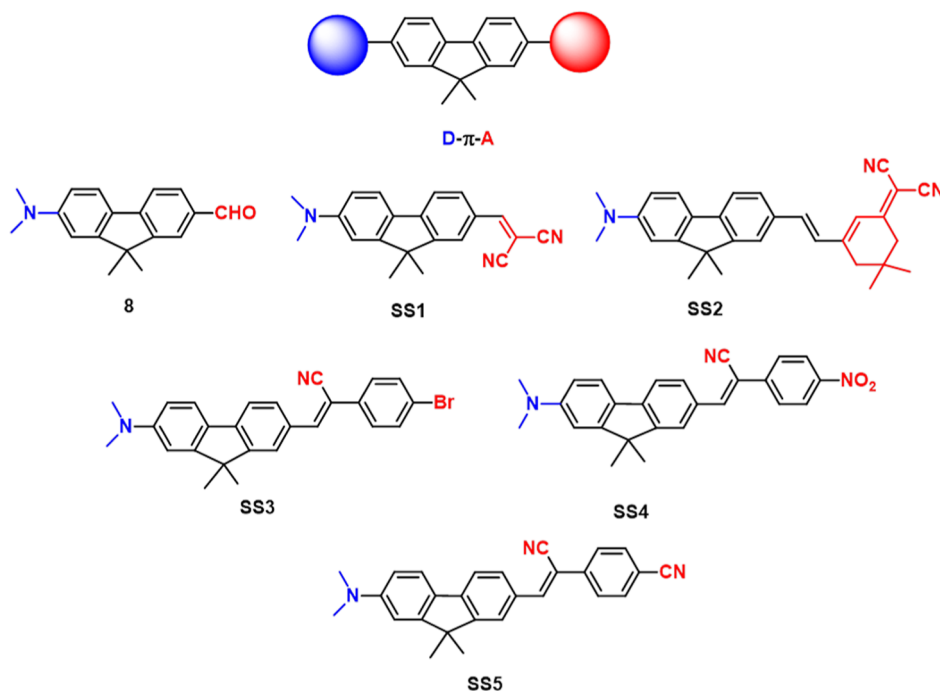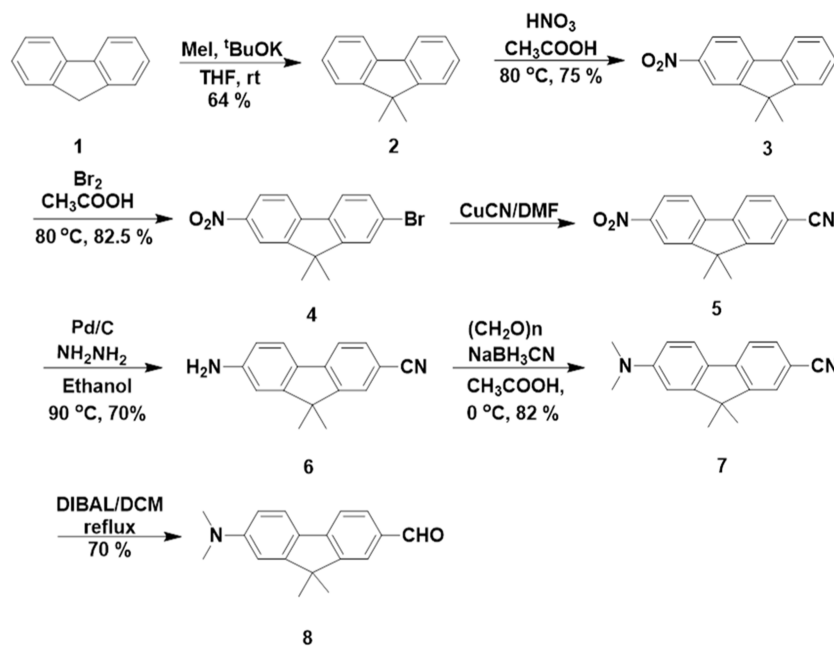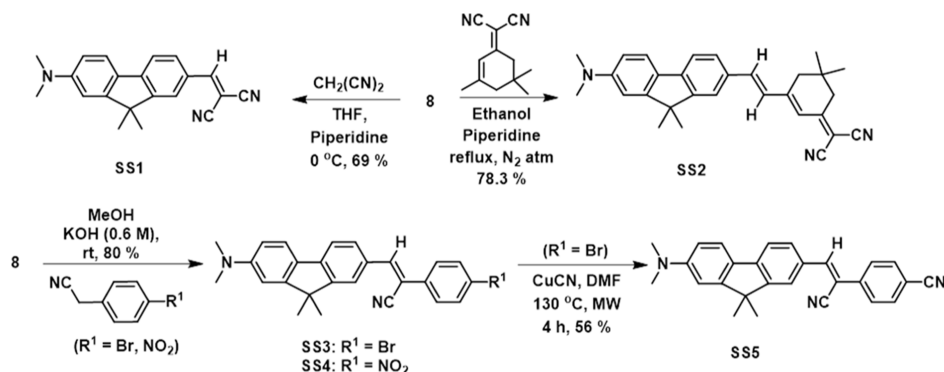

Figure 2. Design strategy for D−π−A chromophores based on the fluorene units and structures of different chromophores.

Scheme 1. Synthetic Outline for the Synthesis of the Common Intermediate 8

Scheme 2. Synthetic Outline of the Linear Chromophores SS1−SS5

80%), respectively (Scheme 2, see the Experimental Section in the Supporting Information).

Meanwhile, microwave-assisted nucleophilic substitution of Br in **SS3** with CuCN yielded (*E*)-4-(1-cyano-2-(7-(dimethylamino)-9,9-dimethyl-9*H*-fluoren-2-yl)vinyl)benzonitrile (**SS5**, 56%). All compounds were fully characterized using spectroscopic data (Figures S1–S30, see the Supporting Information). An unambiguous proof of the structure of **SS3** and **SS4** was obtained by recording single-crystal X-ray structure determination.

2.1. X-ray Crystallographic Characterization. Crystals of **SS3** and **SS4** suitable for single-crystal X-ray analysis were obtained by slow evaporation of the saturated solutions of the compounds in dichloromethane (DCM) layered at the top by light petroleum ether. The ORTEP diagrams of **SS3** (CCDC number 2113758) and **SS4** (CCDC number 2113759) along with atomic numbering are presented in Figure 3. The lattice parameters and other crystallographic data of the crystals are summarized in Table S1, see the Supporting Information. Compounds **SS3** and **SS4** crystallized in the triclinic crystal system with the $P\bar{1}$ space group (Table S1, see the Supporting Information) and are centrosymmetric in the solid state. Therefore, these chromophores are not expected to show bulk

NLO response, and only when incorporated into a suitable noncentrosymmetric matrix, these could show bulk nonlinear susceptibility. However, being inherently dipolar species, a pronounced NLO response at the molecular level was expected. In the crystal packing diagrams of **SS3** and **SS4** (Figure 4), antiparallel molecular dimers could be seen in the unit cells, and the most relevant intermolecular contacts (H-bonding, aromatic CH−π interaction, and shortest centroid-to-centroid distances in Å) are shown. In the three-dimensional crystal packing, the molecules assembled in such a way that the phenyl rings of the cyanostilbene units of one member of the dimeric ensemble were nearly perpendicular to the fluorene units of the neighboring molecules (Figure 4C,D). The fluorene units of all molecules, however, were coplanar and arranged in columns along the *b*-axis.

The molecules in the dimer of **SS3** in the unit cell are held by the strong (3.144 Å, Figure 4A) intermolecular CH−π interactions between the phenyl ring of the stilbene unit and the CH of fluorene units. Likewise, hydrogen bonding (4.126 Å) involving Br and H atoms of the methyl group of N(CH$_3$)$_2$ of each member of the dimer in **SS3** was also observed. Similarly, **SS4** also displayed a supramolecular architecture because of the H-bonding interaction (3.140 Å) between the
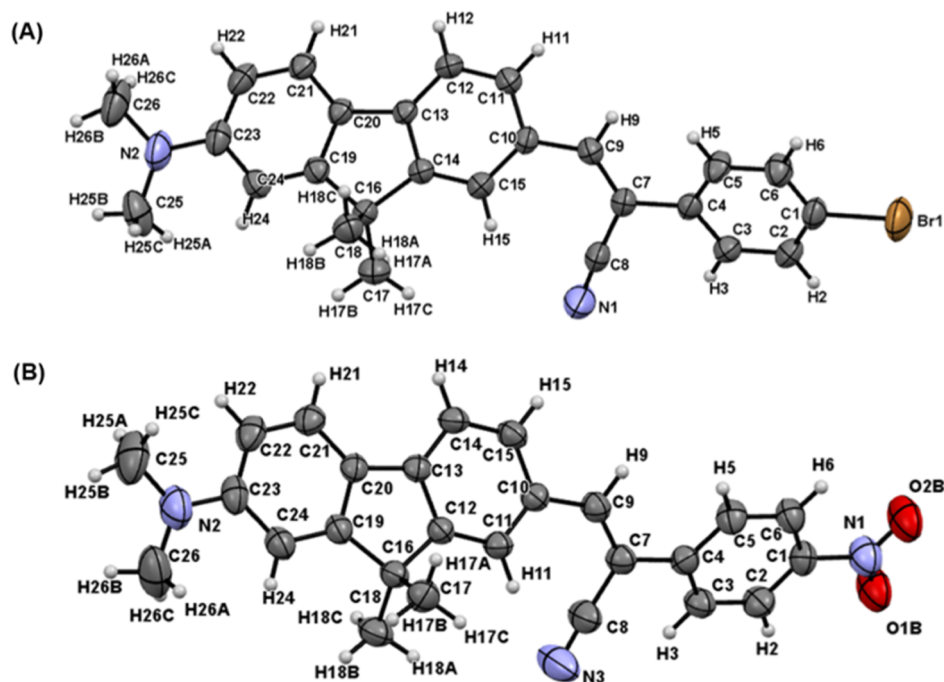
Figure 3. ORTEP view of single-crystal structures of compounds (A) **SS3** and (B) **SS4** with atom labeling scheme (the thermal ellipsoids are drawn at 50% probability level).
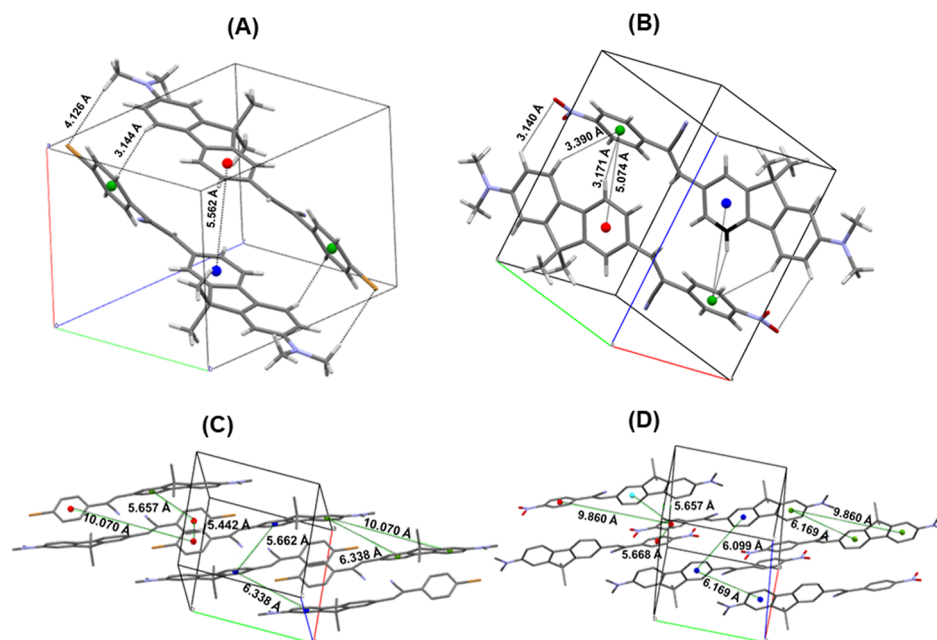

Figure 4. Crystal packing of **SS3** (A) and **SS4** (B) showing intermolecular contacts (H-bonding, aromatic CH−π interaction, and shortest centroid-to-centroid distances in Å) of the antiparallel molecular dimers in the unit cells. Extended crystal packing diagrams of **SS3** (C) and **SS4** (D) viewed along the *c*-axis depicting stacking of the molecular dimers.

NO_2 group of the acceptor of one molecule and the CH of the fluorene aromatic ring of the other molecule (Figure 4B). Additionally, it exhibited a strong CH−π interaction (3.171, 3.390 Å) between the phenyl ring of the stilbene and the CH of the fluorene units. At the same time, the crystal packing forces arising from an effective overlap of the acceptor units (*p*-Br-C_6H_4 in **SS3** and *p*-NO_2-C_6H_4 in **SS4**) with the donor *N,N*-dimethyl aryl units in the crystal packing suggest a positive contribution toward the β_{HRS} of these compounds. Further, the interactions represented by short distances (Figure 4C)

between two stacks of antiparallel pairs of **SS3** (5.662 Å between the closest phenyl rings of the fluorene units of two adjoining pairs and 5.657 Å between the nearest fluorene phenyl ring and *p*-Br-C_6H_4 ring of the adjoining pairs) and identical interdimer interactions in **SS4** (Figure 4D) facilitate supramolecular staggered packing of the molecular asymmetric pairs in the crystal structure. These interdimer supramolecular interactions lead to the stabilization of the molecules and restrict the molecular rotations inhibiting the nonradiative energy dispersion.

2.2. Photophysical Properties. *2.2.1. Linear Optical Behavior.* The absorption spectra of the chromophores **8** and **SS1−SS5** recorded in DCM are shown in Figure 5.
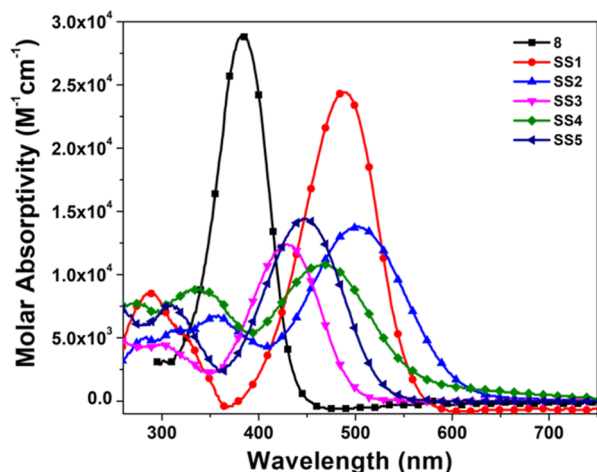

Figure 5. Electronic absorption spectra of chromophores **8** and **SS1−SS5** (1×10^{-5} M) recorded in DCM.

Chromophores **SS1−SS5** showed intense low-energy (LE) bands peaking in the range 428−502 nm and a less intense high-energy (HE) band with wavelengths of maximum absorbance (λ_{max}) in the range 288−356 nm (Table 1). The molecular structures of the chromophores were optimized using the B3LYP/6-31G(d,p) basis set for each chromophore. The calculated electronic transitions and their relative contribution and oscillator strength are listed in Table S2 in the Supporting Information. For better visualization of the absorption data, the spectra were resolved using band fitting analysis (Table 1 and Figure S31, see the Supporting Information). The LE bands are attributed to ICT/donor−acceptor (D → A) transitions originating from the *N,N*-dimethyl aryl donor group to the acceptors and are contributed by HOMO → LUMO transitions. The HE bands were dominantly $\pi \to \pi^*$ transitions (*vide infra*) between an occupied (HOMO + 1, HOMO) π-orbital located on the *N,N*-dimethylaminofluorene unit and the LUMO and/or LUMO +

1 energy levels (Table S2, see the Supporting Information) localized mainly on the π-conjugated path as well as the acceptor (Figure S32, see the Supporting Information). From the orbital energy-level diagram (Figure 6), it is clear that the
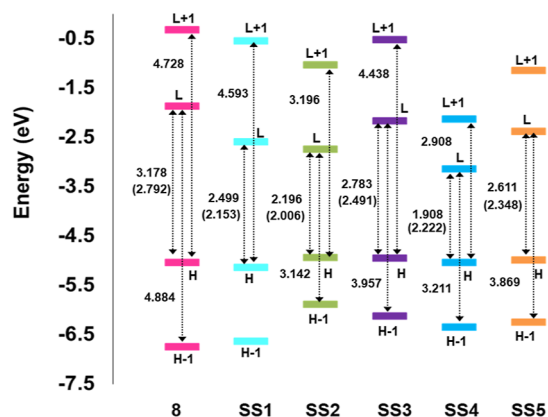

Figure 6. FMO energy-level diagram of **8** and **SS1−SS5** showing HOMO−LUMO gap energies (eV) deduced from DFT calculations [B3LYP/6-31G(d,p)/CPCM model in DCM]. Experimental optical gap (eV) values are given in parentheses.

LUMO energy levels are more affected than the HOMOs upon altering the π-conjugation length as well as the strength of the acceptor. Chromophore **8** showed a broad absorption band centered at 384 nm, assigned as D → A transition, comprising two bands at 335 and 385 nm (resolved using Origin Pro 8.5, Table 1). Further, probing the influence of the electron-acceptor strength on the energies of the molecular orbitals involved in the transitions associated with HE and LE bands, it can be seen (Figure 6 and Tables 2 and S3, see the Supporting Information) that replacing the formyl group of **8** with the dicyanovinyl group in **SS1** (HE band: 288 nm, LE band: 488 nm) not only lowers the energy of the LUMO orbitals, significantly, but also stabilizes the HOMO orbitals, resulting a decrease in energy gap from 2.79 eV (**8**) to 2.15 eV (**SS1**) (Table 2). On moving from **SS1** → **SS2**, both the HE and LE bands exhibited bathochromic shifts of 68 and 14 nm, respectively (Table 1), which reflected the combined effect

Table 1. Electronic Absorption (Experimental, Band-Fitted, and Theoretical) Bands, Emission Bands, and Quantum Yield of 8 and SS1−SS5 in DCM

	λ_{exp} (nm)[a,b]		λ_{fit} (nm)[c]		λ_{theor} (nm)[d]		λ_{em} (nm)[e]	Φ_F (%)
	HE	LE	HE	LE	HE	LE		
8	384 (29.0)		335	385	345	421	491	37
			$[\pi \to \pi^*]$	[D → A]				
SS1	288 (8.5)	488 (24.4)	285	484	301	527	632	43
	$[\pi \to \pi^*]$	[D → A]						
SS2	356 (6.7)	502 (13.8)	341	504	343	624	780	65
	$[\pi \to \pi^*]$	[D → A]						
SS3	301 (4.6)	428 (12.4)	290	427	342	495	586	18
	$[\pi \to \pi^*]$	[D → A]						
SS4	340 (9.0)	468 (10.8)	328	467	371	717	512	38
	$[\pi \to \pi^*]$	[D → A]						
SS5	310 (7.6)	448 (14.4)	308	446	352	527	634	20
	$[\pi \to \pi^*]$	[D → A]						

[a]Recorded at (1×10^{-5} M) in DCM. [b]ε (10^3 M^{-1} cm^{-1}) are shown in parentheses and assignments are shown in square brackets. [c]Band fitting (using Origin Pro 8.5). [d]Calculated *via* time-dependent-density functional theory (TD-DFT) at the B3LYP/6-31G (d,p)/CPCM model in DCM as a solvent (Gaussian 09). [e]λ_{ex} at 290, 450, 480, 420, 450, and 450 nm for **8**, **SS1**, **SS2**, **SS3**, **SS4**, and **SS5**, respectively, in DCM.

Table 2. Calculated HOMO−LUMO Energy of the LE Bands, Optical Gaps, and Electrochemical Data of 8 and SS1−SS5

		TD-DFT calculations (DCM/gas phase)[a]			experimental data			
	E_{ox}^{onset}	E_{HOMO} (eV)	E_{LUMO} (eV)	E_g (eV)	E_{HOMO} (eV)[b]	E_{LUMO} (eV)[c]	E_g^{opt} (eV)[d]	λ_{edge} (nm)[e]
8	0.69	−5.05/−5.05	−1.91/−1.87	3.14/3.18	−5.09	−2.30	2.79	444
SS1	0.79	−5.14/−5.11	−2.59/−2.61	2.54/2.51	−5.19	−3.04	2.15	576
SS2	0.62	−4.93/−4.94	−2.73/−2.745	2.21/2.19	−5.02	−3.01	2.01	618
SS3	0.67	−4.98/−4.96	−2.04/−2.18	2.94/2.78	−5.07	−2.58	2.49	498
SS4	0.65	−5.02/−5.05	−3.17/−3.14	1.85/1.91	−5.05	−2.83	2.22	558
SS5	0.63	−4.98/−5.00	−2.39/−2.39	2.58/2.61	−5.03	−2.68	2.35	528

[a]Using B3LYP/6-31G(d,p) level. [b]Calculated as $E_{HOMO} = -e[E_{ox}^{onset} + 4.4]$. [c]Calculated as $E_{LUMO} = E_g^{optical} + E_{HOMO}$. [d]Calculated as $E_g^{opt} = 1239.84187/\lambda_{edge}$. [e]Recorded in DCM ($1 \times 10^{-5}$ M).

of longer π-conjugation path and the acceptor strength. This was corroborated by the smaller magnitude of the optical gap[28] (2.01 eV) in **SS2** compared to **SS1** due to the change in both HOMO and LUMO levels (Table 2 and Figure 6).

Further, the HE bands as well as the LE bands of **SS3**, **SS4**, and **SS5** were blue-shifted (HE, $\Delta\lambda$ = 55, 16, and 46 nm, respectively; LE, $\Delta\lambda$ = 74, 34, and 54 nm, respectively) in comparison to **SS2**. However, within the group of mutually comparable, cyanostilbene-based chromophores **SS3**, **SS4**, and **SS5**, a pronounced red shift in the HE bands ($\Delta\lambda$ = 39 nm, **SS3** → **SS4**; $\Delta\lambda$ = 9 nm, **SS3** → **SS5**; and $\Delta\lambda$ = 30 nm, **SS5** → **SS4**) and LE bands ($\Delta\lambda$ = 40 nm, **SS3** → **SS4**; $\Delta\lambda$ = 20 nm, **SS3** → **SS5** and **SS5** → **SS4**; Table 1) reflected the effect of the increased acceptor strength, which was corroborated by the optical gap order: **SS3** > **SS5** > **SS4**, the nitro-substituted derivative **SS4** had the lowest HOMO−LUMO gap (Figure 6) and was also most bathochromic (Table 1). The experimental absorption data showed good correlation with the theoretically calculated (Table 1) spectral data.

In such D−π−A chromophores, the position of the ICT bands usually show greater variation upon increasing the acceptor strength compared to the $\pi \to \pi^*$ HE transitions.[29] Interestingly, the position of the absorption maxima of both the HE and LE bands of **SS1**−**SS5** did not show a regular trend in their position upon altering the acceptor strength. This is suggestive of greater mixing of transitions, leading to HE and LE bands as could also be inferred upon visualization of the contour plots of the contributing orbitals (Figure S32, see the Supporting Information). Thus, while LE transitions could be characterized as purely D → A transitions, the HE bands were $\pi \to \pi^*$ with some D → A characteristic also. It is clear that the HOMO−LUMO gap is modulated by both the length of the π-conjugation and the strength of the acceptor.

2.2.2. Emission Behavior of Chromophores. The emission spectral behavior of chromophores displayed in Figure 7 depicts features mirroring the absorption spectral behavior (Figure 5). Unlike absorption spectra, the emission spectral patterns of the chromophores were red-shifted on increasing the length of the π-conjugation spacer and/or the strength of the acceptor linked to the dimethylamino fluorene unit supporting the operation of strong ICT. Chromophore **SS2** showed the maximum red shift with the longest emission wavelength λ_{em} = 780 nm, followed by **SS5** (λ_{em} = 634 nm), **SS1** (λ_{em} = 632 nm), **SS3** (λ_{em} = 586 nm), and **SS4** (λ_{em} = 512 nm). The emission wavelength of the shortest chromophore bearing a CHO acceptor **8** was the lowest (λ_{em} = 491 nm).

2.3. Solvatochromism. No regular trend in the position of the absorption bands was noticed when the absorption spectra of **SS1**−**SS5** and **8** were recorded in solvents of varying polarity (Figures 8a and S33−S38 and Tables 3 and S4, see the
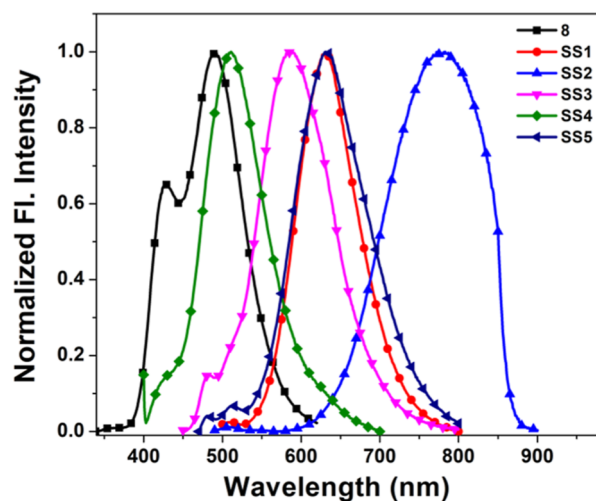

Figure 7. Normalized emission spectra of chromophores **8** and **SS1**−**SS5** (1×10^{-5} M) recorded in DCM.

Supporting Information), except for a slight blue shift in the LE bands of **SS1**−**SS5**, recorded in methanol (Figures S33−S38, see the Supporting Information). Although the presence of the donor and acceptor moieties in the dyads ensures the ground-state charge asymmetry, the solvent-dependent linear optical behavior **SS1**−**SS5** pointed to insignificant solvatochromism, which meant a less-polar ground state of the molecules. The more polar and hydrogen bonding solvent methanol may however stabilize the molecules in the ground state, which accounts for the observed negative solvatochromism albeit of very small magnitude (Table 3). Dependence of the absorption maxima for the ICT bands of **SS1**−**SS5** on the dielectric constant of the solvent is plotted (Figure S39a, see the Supporting Information), wherein very irregular changes in the position of ICT maxima were seen in solvents of different dielectric constant, attesting to the lack of a distinctive positive solvatochromism.

Probing the influence of the solvent polarity on the excited state of the compounds, significant shifts in the position of the emission bands in the fluorescence emission spectra were noted when the spectra were recorded in solvents of varying polarity (Figures 8b and S39b, see the Supporting Information). This meant (i) more polar excited states of these chromophores, (ii) a large difference in polarity and dipole moments of the ground and excited states, which was also confirmed by the dipole moments data computed by using TD-DFT calculations using the CPCM solvation model (Table S5, see the Supporting Information), (iii) existence of strong ICT and the LE band preferably stabilized by the solvating
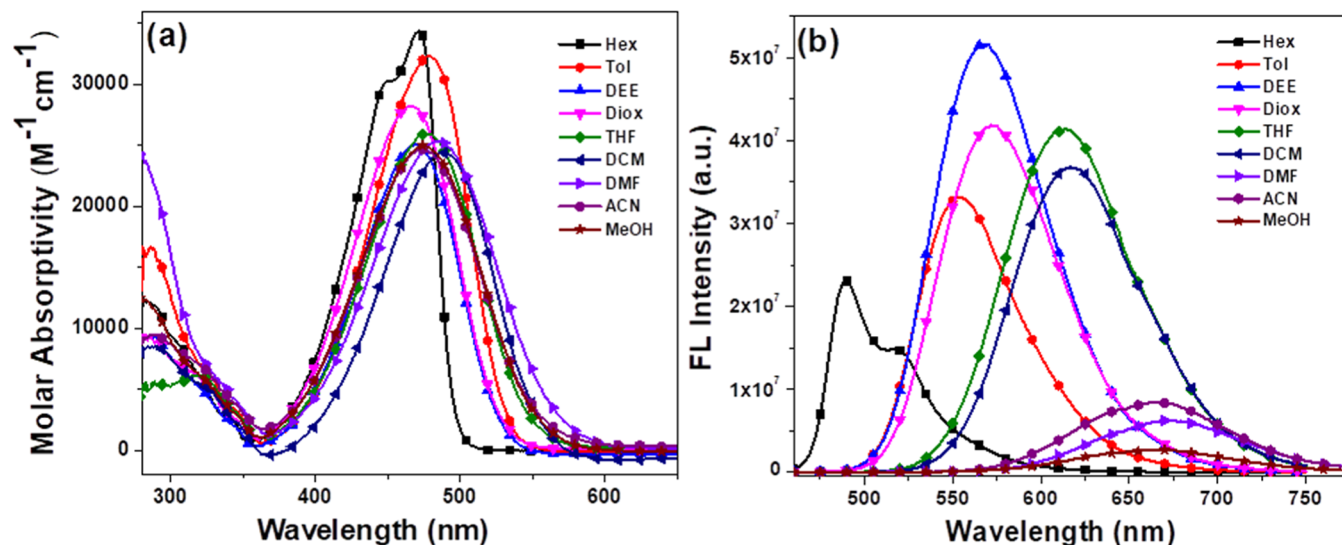
Figure 8. (a) UV−visible absorption and (b) emission behavior of **SS1** (1×10^{-5} M) in different solvents.

Table 3. Optical Properties of 8 and SS1−SS5 in Different Solvents

	solvent	polarizability factor[a] (Δf)	λ_{abs} (nm)[b]	extinction coeff (ε_{max}) (M^{-1} cm^{-1})	λ_{em} (nm)[b]	Stokes shift (nm)	quantum yield[c] (Φ_F)	fluorescence lifetime (τ_F) (ns)[d]	radiative rate (k_r) (s^{-1})[e]	nonradiative rate (k_{nr}) (s^{-1})[f]
8	toluene	0.01	376	30 700	434	58	0.27	1.90	1.42×10^8	3.71×10^8
	DCM	0.22	384	29 000	490	106	0.37	2.69	1.37×10^8	2.34×10^8
	MeOH	0.31	382	29 150	534	152	0.13	1.87	0.69×10^8	4.65×10^8
SS1	toluene	0.01	478	32 300	554	76	0.42	1.20	3.31×10^8	4.57×10^8
	DCM	0.22	488	24 400	632	130	0.43	2.85	1.51×10^8	2.00×10^8
	MeOH	0.31	475	25 000	668	193	0.11	2.10	0.52×10^8	4.23×10^8
SS2	toluene	0.01	502	14 500	629	127	0.57	1.49	3.82×10^8	2.89×10^8
	DCM	0.22	502	13 800	780	228	0.65	2.19	2.97×10^8	1.59×10^8
	MeOH	0.31	490	13 600	707	217	0.04	1.64	0.24×10^8	5.85×10^8
SS3	toluene	0.01	430	18 000	520	90	0.21	1.59	1.32×10^8	4.97×10^8
	DCM	0.22	428	12 400	586	146	0.18	1.76	1.02×10^8	4.66×10^8
	MeOH	0.31	422	11 100	605	183	0.13	1.29	1.00×10^8	6.74×10^8
SS4	toluene	0.01	452	12 800	598	146	0.26	0.45	5.78×10^8	1.64×10^8
	DCM	0.22	468	10 800	512	151	0.38	2.69	1.41×10^8	2.30×10^8
	MeOH	0.31	456	11 500	558	102	0.09	2.38	0.38×10^8	3.82×10^8
SS5	toluene	0.01	450	13 300	558	108	0.21	1.35	1.56×10^8	5.85×10^8
	DCM	0.22	448	14 400	634	165	0.20	1.78	1.12×10^8	5.50×10^8
	MeOH	0.31	436	10 900	662	226	0.24	0.55	4.36×10^8	1.38×10^9

[a]Lippert orientation polarizability factor, $\Delta f = (\varepsilon - 1)/(2\varepsilon + 1) - (\eta^2 - 1)/(2\eta^2 + 1)$, where ε is the dielectric constant and η is the refractive index, (ref 32). [b]DCM (1×10^{-5} M). [c]$\Phi_F = [(F_s/F_r) \times (1 - 10^{A_r})/(1 - 10^{A_s}) \times (\eta_s^2/\eta_r^2)] \Phi_r$, where F_s and F_r are the area of emission band of the chromophore and fluorescein used as a reference, A_s and A_r are the absorbance of chromophore and reference, η_s and η_r are the refractive index of solvent for chromophore and reference, and Φ_r is the quantum yield of reference (0.95 in 0.1 M aqueous NaOH). [d]DCM (1×10^{-5} M) excited at different excitation wavelengths (Table S8, see the Supporting Information). [e]$k_r = \Phi_F/\tau_F$. [f]$k_{nr} = (1 - \Phi_F)/\tau_F$.

effect of the polar solvent, and (iv) a high optical nonlinearity (β, first hyperpolarizability) (*vide infra*). The calculated HOMO−LUMO levels indicated that the strong solvatofluorochromism arises from the ICT, wherein the ground state has significant localization of the electron density on the donor, *N,N*-dimethylamino part of the chromophores, while it shifts to the acceptor unit in the excited state (Figure S32, see the Supporting Information). In addition to the bathochromic shift in the emission bands, upon increasing solvent polarity, the emission intensities saw a diminishing trend (Table S6, see the Supporting Information).

Thus, maximum luminescence was noted in the least polar hexanes or toluene, which was nearly quenched in methanol. The emission spectra recorded in methanol exhibited

negligible fluorescence with quantum yields (Φ_F) not exceeding the value of 0.24 (Tables S6 and S7, see the Supporting Information) compared to the highest quantum yield ($\Phi_F = 0.65$) of **SS2** in DCM. This is attributed to the enhanced ICT, leading to nonradiative relaxation[30] (Tables 3 and S7, see the Supporting Information), which results in fluorescence quenching due to the increased probability of nonfluorescent twisted ICT state population in methanol (Figures S33−S38, see the Supporting Information). The evidence for the existence of a relaxed twisted ICT state in D−A chromophores has been demonstrated by means of femtosecond time-resolved fluorescence measurements.[30,31]

Time-correlated single-photon counting measurements showed that as the solvent polarity increased, the fluorescence

lifetimes also increased from 0.45 to 1.90 ns in nonpolar toluene to 1.76−2.85 ns in moderately aprotic polar DCM (Table 3). However, in protic solvent, an opposite trend was noticed; that is, as the polarity increases from DCM to methanol (MeOH), a decrease in the fluorescence lifetime is observed (Tables 3 and S8 and Figures S33−S38, see the Supporting Information), which attributed to the hydrogen bonding in methanol. Further, the radiative rates (k_r) showed a significant decrease; in turn, the nonradiative rates (k_{nr}) saw an increase with increasing solvent polarity (Table 3).[33]

To further ascertain the strong ICT characteristic, quantitatively, the excited-state dipole moments were calculated using the Lippert−Mataga relation (eq 1),[32] representing the relation between Stokes shift and solvent polarity parameters. Equation 1 is an approximation in which solute polarization and high degrees of linearity are neglected; therefore, the estimations of the excited-state dipoles are considered as reliable.

$$\overline{\nu}_A - \overline{\nu}_F = \Delta\overline{\nu} = \frac{2}{hca_o^3}\left(\frac{\varepsilon - 1}{2\varepsilon + 1} - \frac{n^2 - 1}{2n^2 + 1}\right)(\mu_e - \mu_g)^2$$
$$= \frac{2\Delta f}{hca_o^3}\Delta\mu^2 \qquad (1)$$

In eq 1, $\overline{\nu}_A$ and $\overline{\nu}_F$ are wavenumbers in cm^{-1} corresponding to the wavelengths of the maximum absorption and emission, h is Planck's constant, c is the speed of light, and a_o is the Onsager cavity radius. The parameters ε and n represent the relative permittivity and refractive index, respectively, and are considered in the orientation polarizability term, Δf.

It is known that the difference in dipole moments in the ground and the excited states can be used to analyze the solvent sensitivity to polarity.[34] Owing to the least solvent interactions, the estimated changes in dipole moment ($\Delta\mu_{eg}$) are appreciably large. Figure 9 shows the plot of the Stokes
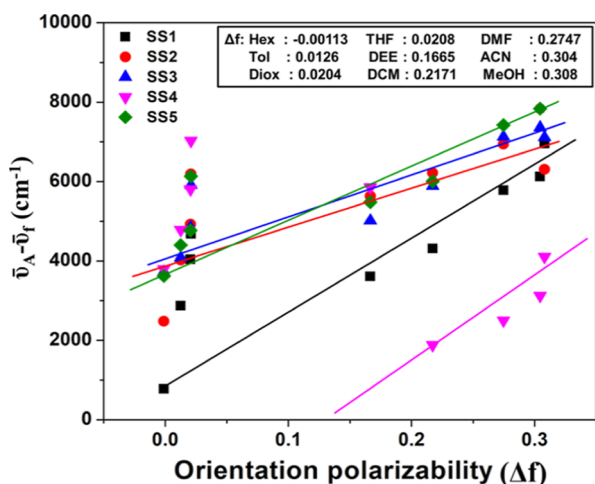

Figure 9. Relation between the Stokes shift ($\overline{\nu}_A - \overline{\nu}_F$) and the orientation polarizability (Δf).

shift of chromophores versus orientation polarizability (Δf). These figures indicated the presence of charge transfer excited state in these chromophores.

2.4. Thermal Stability. Due to their dense molecular packing and the stacking arrangement in the solid state, complemented by intermolecular forces, chromophores **SS1**−**SS5** were expected to have good thermal stability. All

chromophores showed very good stability to heat (Table 4) in thermogravimetric analysis (TGA) with the onset temperature falling above 325 °C, after which a significant weight loss was observed (Figure S40, see the Supporting Information). The excellent thermal stability is a good attribute for the fabrication of optoelectronic devices.

2.5. Electrochemistry. The redox behavior of chromophores **SS1**−**SS5** (4×10^{-4} M) was studied in DCM solutions by cyclic voltammetry (CV) with tetra-n-butyl ammonium hexafluorophosphate (TBAPF$_6$) as the supporting electrolyte. A platinum electrode was used as a counter electrode, glassy carbon was used as the working electrode, and Ag/AgCl was used as the reference electrode. Ferrocene was used as an internal reference, and the voltammograms were recorded at a scan rate of 100 mV s^{-1}. Variation in the scan rates did not affect the peak potentials and/or $E_{1/2}$ values. The CV spectra (Figure 10) show the redox behavior of all compounds. The calculated energies showed good correlation (Tables 1 and 2) with the corresponding values obtained from CV and UV−visible absorption data. All chromophores showed first oxidation potential in the range of 0.74−0.91 V (Figure 10), attributed to the loss of electron from the N,N-dimethylamine subunit, while the second oxidation potential corresponded to the oxidation of fluorene.

Comparison of the electrode potentials allowed visualization of the effect of strength of the acceptor and/or π-conjugation path length connecting the donor and the acceptor in chromophores **SS1**−**SS5** and **8**. The first oxidation potentials of chromophores **8** (E_{pa}, 0.87 V) and **SS1** (E_{pa}, 0.91 V) were marginally higher (Table 4) compared to **SS2** (E_{pa}, 0.74 V). This is attributed to the facile oxidation of **SS2**, which could be attributed to the longer π-conjugation path length, weakening the communication between the donor N,N-dimethylamino group and the acceptor. The dicyanovinylidene group in **SS1** exerts a stronger electron-withdrawing effect, more than the formyl group in **8**, rendering the first oxidation more difficult in the former. The second oxidation potentials of the compounds, corresponding to the removal of electron from the fluorene unit, are significantly higher (Table 4).[35]

While a single peak corresponding to the reduction of the acceptor unit was observed in **8**, **SS1**, and **SS2**, an additional peak was observed for the chromophores **SS5** containing a cyanostilbene acceptor (Figure 10), which may arise due to the formation of radical anion and/or a dianionic species upon reduction. Further, the second oxidation potential in the case of compound **SS4** is slightly higher than that of the comparable members **SS5** and **SS3** (Table 4).

Natural bond orbital (NBO) calculations showed net positive charge on the donor N,N-dimethylamino as well as the 9,9-dimethyl fluorene (linker) groups while net negative charge on the acceptor unit (Table 5 and Figure S41, see the Supporting Information), which corroborated the path of electron transfer (ET) in **8** and **SS1**−**SS5**. Likewise, positive charge on the linker suggested the dominating role of the linker in the ET in **8** and **SS1**−**SS5**. Interestingly, the negative charges on the acceptor units in **SS3**−**SS5** are in the same order as the first oxidation potentials, suggesting the nitro-substituted **SS4** to be the most bathochromic, which indeed is as revealed from the UV−visible absorption data (Table 1). The distinctive separation of positive charge on the donor and linker and negative charges on the acceptor units in **SS1**−**SS5** renders these compounds to be purely dipolar compounds

Table 4. Electrochemical and Decomposition Temperatures for 8 and SS1−SS5 in DCM

	E_{ox}^{onset}	E_{red}^{onset}	E_{pa1} (V)[a]	E_{pa2} (V)[a]	E_{pc1} (V)[a]	i_{pa1} (A) (10^{-6})[b]	i_{pa2} (A) (10^{-6})[b]	i_{pc1} (A) (10^{-5})[b]	T_d (°C)[c]
8	0.69	−0.76	0.87	1.56	−1.06	7.12	9.60	−1.88	235
SS1	0.79	−0.82	0.91	1.50	−1.12	2.97	4.83	−2.05	272
SS2	0.62	−0.85	0.74	1.41	−1.23	2.55	3.80	−1.89	240
SS3	0.67	−0.85	$E_p^f = 0.79; E_p^r = 0.70$[d]	1.50	−1.19	3.94	6.05	−1.82	265
SS4	0.65	−0.79	$E_p^f = 0.82; E_p^r = 0.71$[d]	1.52	−1.09	4.58	2.91	−2.11	315
SS5	0.63	−0.83	$E_p^f = 0.79; E_p^r = 0.69$[d]	1.51	−1.14 (−1.59)[e]	8.98	7.71	−1.67 (−2.53)[f]	335

[a]E_{pa} and E_{pc} correspond to the anodic and cathodic peak potentials, respectively; scan rate 100 mV s^{-1}. [b]Amplitudes of the anodic and cathodic peaks. [c]Corresponding to a 10% weight loss (TGA). [d]E_p^f and E_p^r are forward and reverse peaks for the reversible redox process. [e]Second cathodic peak potential (E_{pc2}). [f]Amplitude of second cathodic peak (i_{pc2}).
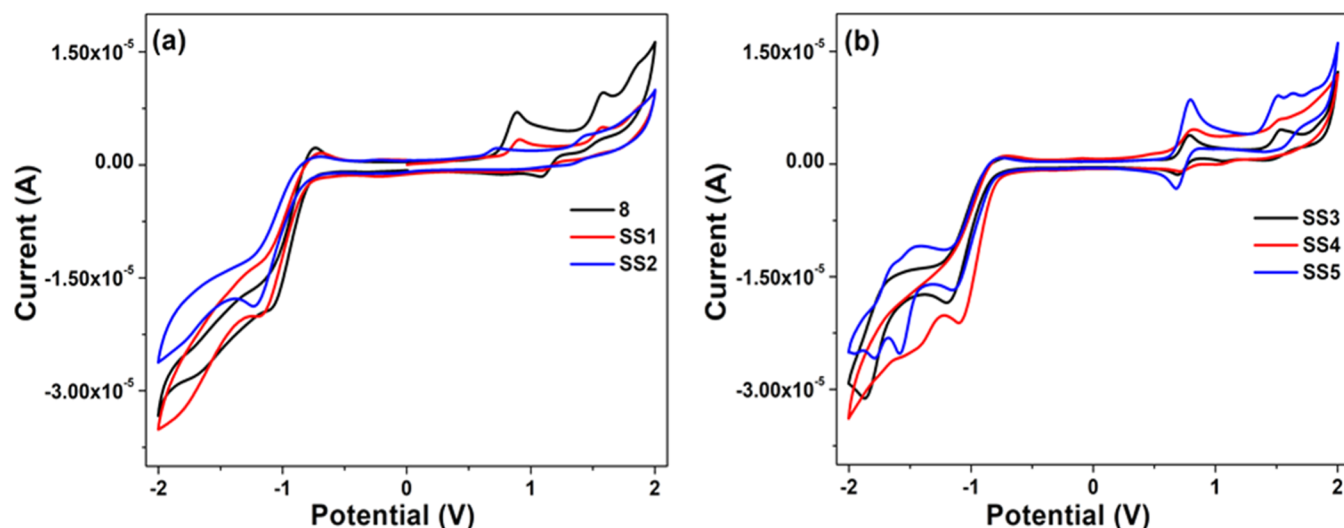

Figure 10. Cyclic voltammograms of (a) **8**, **SS1**, **SS2**, and (b) **SS3−SS5** (4×10^{-4} M) in DCM.

Table 5. Estimated Natural Bond Orbital (NBO) Charge Distribution of 8 and SS1−SS5

	NBO charge distribution on sub-units		
	donor	π-linker	acceptor
8	0.03043	0.04701	−0.07746
SS1	0.04670	0.17341	−0.22011
SS2	0.02472	0.16134	−0.18606
SS3	0.02735	0.86210	−0.11356
SS4	0.03846	0.13366	−0.17212
SS5	0.01114	0.10432	−0.11546

with a single major dipolar hyperpolarizability tensor component β_{zzz}.

2.6. Quadratic Hyperpolarizability. The first hyperpolarizability, β_{HRS}, for the chromophores **8** and **SS1−SS5**, was measured in DCM using the hyper-Rayleigh scattering (HRS) method. A Q-switched Nd:YAG (Spectra-Physics, repetition rate 10 Hz and pulse width 10 ns) laser at a fundamental wavelength of 1064 nm was used for the measurements. The analysis of the fluorescence emission spectra indicated chances of multiphoton fluorescence (MPF) and resonance enhancement of the second-order nonlinear polarizability values. We performed monochromator scan (for MPF correction, see the Supporting Information) for all the compounds. It was seen

that all compounds except **8** and **SS2** showed a broad MPF band (Figure S42, see the Supporting Information). Therefore, the values were corrected for resonance enhancement and MPF. The β_{HRS} values are tabulated in Table 6. In accordance with two-level model of Oudar and Chemla (eq 2),[36] the principle factors that determine molecular polarization and hence second-order polarizability are the strength of the donor and acceptor and the π-conjugation pathway connecting them.

Table 6. Quadratic NLO Parameters of 8 and SS1−SS5 in DCM

	β_{HRS}[a] $(10^{-30}$ esu)	β_o[b] $(10^{-30}$ esu)	β_{Theor}[c] $(10^{-30}$ esu)	$[\beta_{zzz}^{max}]$[d] $(10^{-30}$ esu)	(β^{int})[e] $(10^{-30}$ esu)
8	74 ± 14	32	125.15	2 087	0.036
SS1	548 ± 40	69	611.81	7 244	0.076
SS2	626 ± 98	53	845.79	11 001	0.057
SS3	274 ± 35	81	372.11	5 716	0.048
SS4	645 ± 48	119	963.46	9 615	0.067
SS5	566 ± 65	136	774.90	7 927	0.071

[a]Second-order nonlinear polarizability (first hyperpolarizability) corrected for resonance/MPF enhancement, β_{HRS} was recorded at 1064 nm in DCM. [b]β_o: frequency-independent static first hyperpolarizability calculated using the equation: $\beta_o = \beta_{HRS}[1 - \lambda_{max}^2/\lambda_{fund}^2][1 - (2\lambda_{max})^2/\lambda_{fund}^2]$. [c]$\beta_{Theor}$: theoretical second-order nonlinear polarizability. [d]$[\beta_{zzz}]^{max} = (3)^{1/4}[eh/(m)^{1/2}]^3 N^{3/2}/E_{10}^{7/2}$, where N is the number of conjugated electrons and E_{10} is the transition energy. [e]β^{int} is the intrinsic off-resonant hyperpolarizability given by $\beta_{HRS}/[\beta_{zzz}]^{max}$.

$$\beta \propto \Delta\mu_{ge} r_{ge}^2 / (E_{ge})^2 \qquad (2)$$

In eq 2, β is the second-order nonlinear polarizability, $\Delta\mu_{ge}$ represents the dipole moment difference between the ground and excited states, and r_{ge} is the transition dipole moment, which can be directly correlated with the oscillator strength (f) or molar extinction coefficient (ε). Finally, E_{ge} represents the optical gap of the ICT (LE) transition.

The trend of β_{HRS} of **8** (β_{HRS} = 74 × 10^{-30} esu, Table 6) with **SS1** (β_{HRS} = 548 × 10^{-30} esu) and **SS2** (β_{HRS} = 626 × 10^{-30} esu) clearly established the role of enhanced acceptor strength (**8**vs**SS1**) and effect of increased π-conjugation path length (**SS1**vs**SS2**). Thus, a systematic 7.4-fold and 8.5-fold increase of β_{HRS}, respectively, in the pairs comprising **8**, **SS1** and **SS1**, and **SS2** demonstrates the effect of the acceptor strength and length of the π-conjugation pathway as the donor group was the same. The increasing order of oscillator strength of the LE transition (f = 0.7642, **8**; 1.0011, **SS1** and 1.2377, **SS2**), the change of dipole moment ($\Delta\mu$ = 9.45 D, **8**; 16.09 D, **SS1** and 23.34 D, **SS2**) between the ground and excited states, and the decreasing optical gap (E_{ge} = 2.79 eV, **8**; 2.15 eV, **SS1** and 2.01 eV, **SS2**) in that order corroborate the order of experimental β_{HRS} values of these three compounds. Likewise, the group of cyanostilbene-based chromophores **SS3**, **SS4**, and **SS5**, in which the acceptor strength increases in the order **SS4** > **SS5** > **SS3** owing to the strength of the electron-withdrawing group (NO_2 > CN > Br) attached at the p-position of the phenyl group, values in the same order (Table 6). Although the oscillator strength of **SS4** (f = 0.6274) was the lowest of the three members, the higher β_{HRS} value of **SS4** is attributed to the higher change in the dipole moment ($\Delta\mu$ = 24.93 D) and lower optical gap (2.22 eV).

The theoretically calculated first hyperpolarizability (β_{Theor}) shows good correlation with the experimental value (Table 6). Considering the robustness of the theoretically calculated values, it could be argued that reliable structure-dependent first hyperpolarizability correlations could be drawn for similar fluorene-based donor−acceptor chromophores for which experimental determinations were not possible due to instability and/or nonaccessibility or cumbersome synthesis. Similarly, frequency-independent static first hyperpolarizability has also been determined and shows a trend similar to the experimental first hyperpolarizability. A histogram showing the first hyperpolarizability of **SS1**−**SS5** and **8** is shown in Figure 11, while the quadratic curves are shown in Figure S43 in the Supporting Information.

The NLO efficiency of compounds can be compared more realistically from the intrinsic (size-independent) hyperpolarizability β^{int}, as defined by Kuzyk.[37] Intrinsic hyperpolarizability is a worthy parameter for device applications, where the bulk susceptibility per unit volume is more important than the molecular hyperpolarizability per chromophore.[38] Interestingly, the trend of β^{int} mirrored that of the experimental β_{HRS} for **8** and **SS1** (Table 6). However, the β^{int} value of **SS2** is smaller than that of **SS1** (Figure 12). This reversed trend can be justified considering the fact that β^{int} is size independent; therefore, the longer length of the π-conjugated spacer in **SS2** would weaken the strength of the acceptor, resulting in lower β_{HRS} compared to shorter chromophore **SS1** but may not exert influence on β^{int}.

Similarly, the CN-substituted **SS5** outperforms in terms of β^{int} than the otherwise stronger NLO chromophore **SS4**. In order to visualize these results in a larger standpoint, the NLO
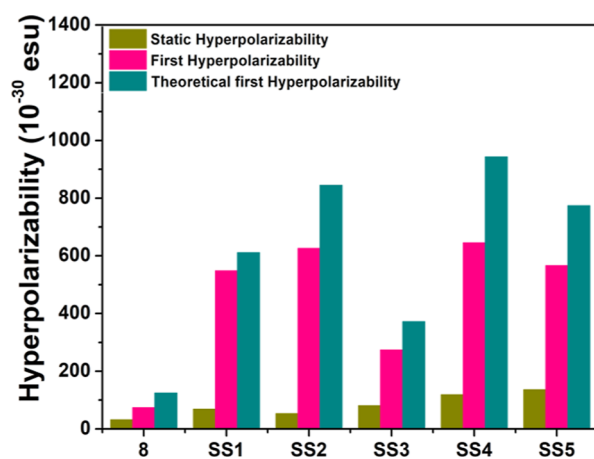

Figure 11. Histogram presents comparison of the different hyperpolarizability parameters for **8** and **SS1**−**SS5**.

behavior of the current set of chromophores has been compared with analogues lacking a linear conjugation **SP1**−**SP5** (Figure 13), reported by us earlier.[27]

The fundamental limit of the intrinsic first hyperpolarizability of the "design-deficient" compounds **SP1**−**SP5** with a "nonlinear conjugation pathway" is defined by **SP5**, Figure 12a. It is apparent that the intrinsic first hyperpolarizability of the "linearly conjugated" counterparts **SS1**−**SS5** except **SS3** is way higher (3.7-fold in **SS4**) than **SP1**−**SP5**. The β^{int} of **SS3** is actually higher than the comparable analogue **SP3**. Further, compounds **SS1**−**SS5** are located on the top right-hand corner of the plot of β^{int}versus wavelength (Figure 12b), whereas the set of chromophores **SP1**−**SP5** is found in the lower left-hand corner of the plot.

The reason for the higher first hyperpolarizability [**SS1**−**SS5**: β_{HRS} 274−645 × 10^{-30} esu, **SP1**−**SP5**: β_{HRS} 113−174 × 10^{-30} esu] and the consequent intrinsic hyperpolarizability [**SS1**−**SS5**: β^{int} 0.048−0.076, **SP1**−**SP5**: β^{int} 0.028−0.050] of the current set of chromophores is attributed to the blue-shifted LE bands [**SS1**−**SS5**: λ_{max} 428−502 nm (LE), **SP1**−**SP5**: λ_{max} 396−458 nm (LE)], lower optical gaps [**SS1**−**SS5**: E_g^{opt} 2.01−2.49 eV, **SP1**−**SP5**: E_g^{opt} 2.239−2.707 eV], higher difference in dipole moments between the ground and excited states [**SS1**−**SS5**: $\Delta\mu_{ge}$ 16.09−24.93 D; **SP1**−**SP5**: $\Delta\mu_{ge}$ 3.098−21.548 D], and higher oscillator strength [**SS1**−**SS5**: f 0.6274−1.2377; **SP1**−**SP5**: f 0.3003−1.0960] of the band contributing to the NLO response.

Likewise, the emission bands of **SS1**−**SS5** were considerably red-shifted (λ_{em} 512−780 nm and Φ_F 18−65%) and intense, while for **SP1**−**SP5**, the emission bands peaked in the range of 478−694 nm and were significantly less intense (Φ_F: 2−14%). In Figure 14, the electrostatic potential maps depicting NBO charges are shown, which clearly show the direction of dipoles in **SS1** and **SS4** and their analogues **SP1** and **SP4** having a "nonlinear" conjugation (Figure S44, see the Supporting Information). Thus, designing chromophores with linear conjugation is a better strategy for obtaining higher NLO response of the fluorene-based donor−π−acceptor chromophores.

3. CONCLUSIONS

This study was aimed to demonstrate the difference in the linear optical properties and NLO response (first hyperpolarizability, β_{HRS}, and the associated intrinsic hyperpolariz-
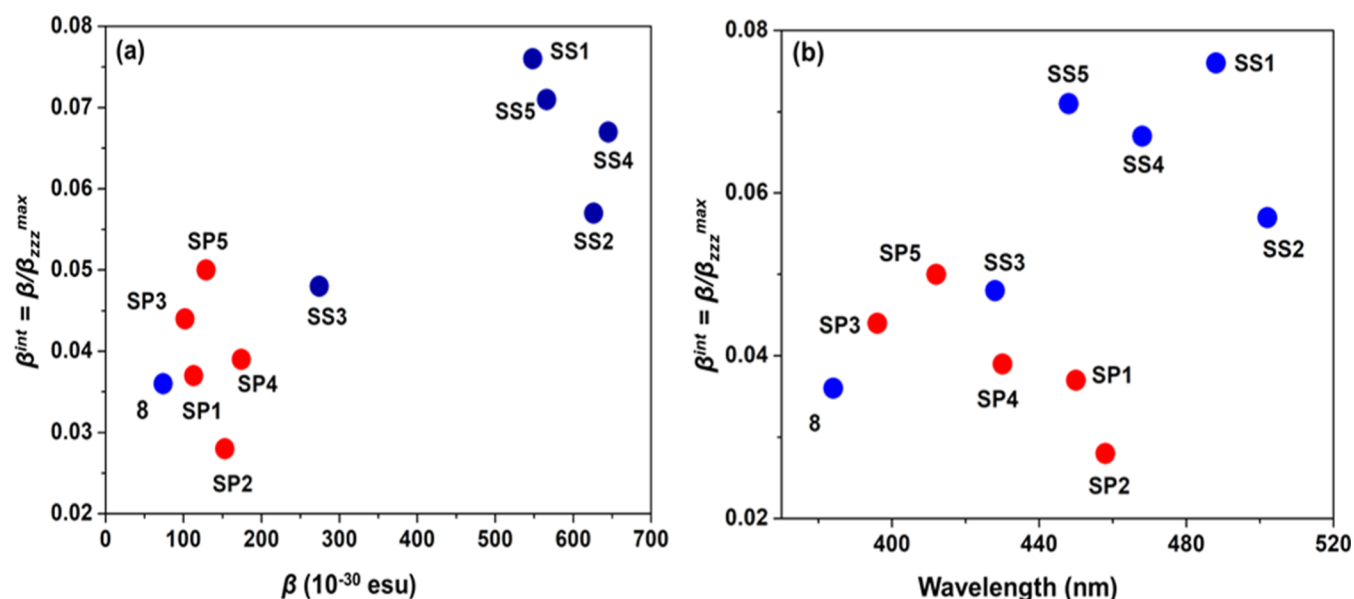
Figure 12. (a) Intrinsic off-resonant hyperpolarizability, β^{int}, as a function of off-resonant hyperpolarizability, β, and (b) β^{int} as a function of wavelength of **8** and **SS1–SS5**.

SP1: $\beta_{HRS} = 113 \pm 5$; $\beta^{int} = 0.037$ **SP2:** $\beta_{HRS} = 153 \pm 9$; $\beta^{int} = 0.028$

SP3: $\beta_{HRS} = 102 \pm 5$; $\beta^{int} = 0.044$ **SP4:** $\beta_{HRS} = 174 \pm 10$; $\beta^{int} = 0.039$ **SP5:** $\beta_{HRS} = 129 \pm 6$; $\beta^{int} = 0.019$
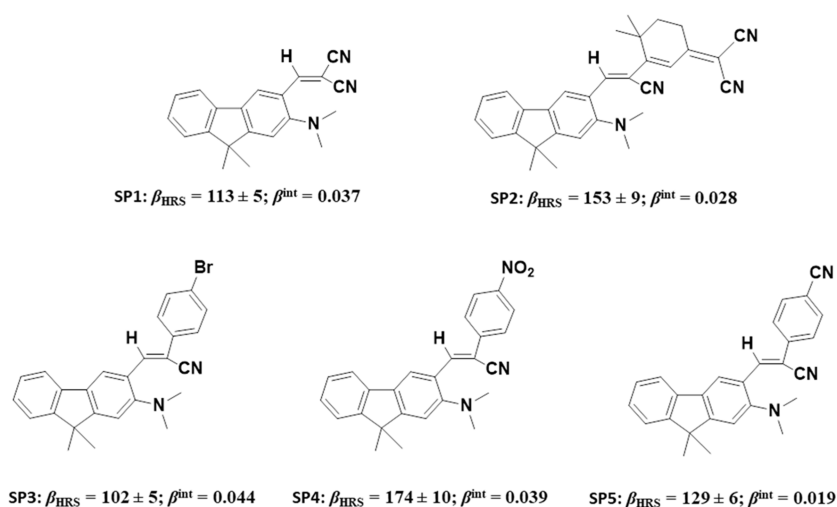
Figure 13. D−π−A chromophores **SP1–SP5** based on the fluorene-bearing "nonlinear" conjugation pathway. The first hyperpolarizability values ($\times 10^{-30}$ esu) and β^{int} are also shown.[27]

ability, β^{int}) of a set of fluorene-based "push−pull" chromophores **SS1–SS5** having a "linear" conjugation path with the corresponding chromophores **SP1–SP5** having "nonlinear" conjugation path. The former set of chromophores showed significantly red-shifted absorption/emission bands, high Stokes shift, and high quantum yield. These chromophores also showed high thermal stability and structure-dependent (strength of donor and acceptor and path of π-conjugation) photophysical and redox behavior. Further, superior first hyperpolarizability, β_{HRS}, of **SS1–SS5** (274 to 645×10^{-30} esu) as well as intrinsic hyperpolarizability β^{int} has been attributed to the lower optical gap (E_g), the oscillating strength of the LE band, and collective influence of the difference in the dipole moment ($\Delta\mu_{ge}$) of the ground and excited states, NBO charges, etc. Apart from the number of delocalized electrons, β^{int} depends on the wavelength of the maximum absorption and the measured first hyperpolarizability. Further, the crystal packing forces due to the effective overlap of the acceptor units (p-Br-C$_6$H$_4$ in **SS3** and p-NO$_2$-

C_6H_4 in **SS4**) with the donor N,N-dimethyl aryl units in the solid state furnished a positive contribution toward the first hyperpolarizability of these compounds. This study has revealed a direct comparison of NLO behavior of two sets of fluorene-based "push−pull" chromophores having difference in conjugation paths and has reasserted the superiority of the "linear" conjugation pathway.

4. EXPERIMENTAL SECTION

4.1. Materials and Instrumentation. The reagents potassium tertiary butoxide (KO^{t}Bu), Pd/C, NaBH$_3$CN, paraformaldehyde, DIBAL, bromine, malononitrile, 4-bromo-phenylacetonitrile, 4-nitrophenylacetonitrile, and the solvents used were bought from Spectrochem, India. Prior to their use in reactions, the solvents N,N-dimethylformamide (DMF), DCM, methanol (CH$_3$OH), and tetrahydrofuran (THF) were dried by using recommended methods.[27]
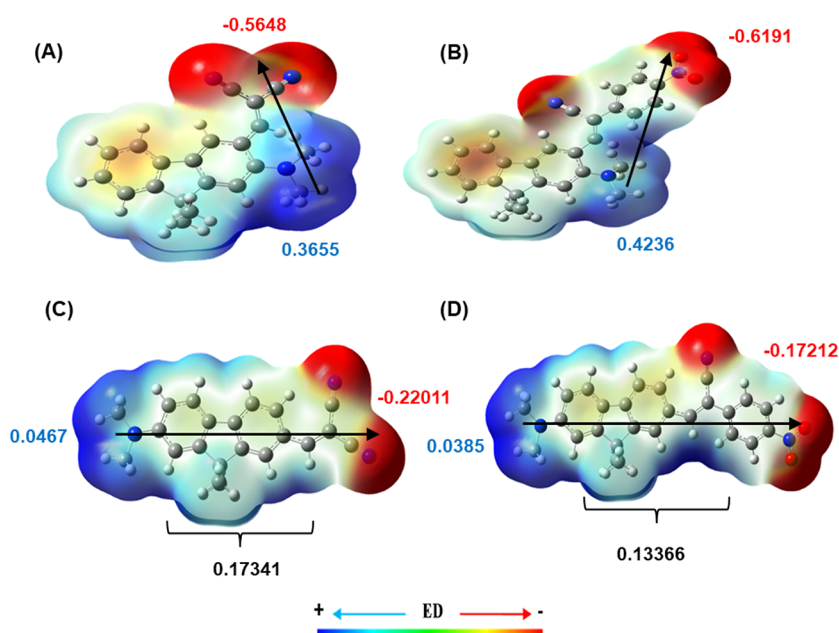
Figure 14. Electrostatic potential maps for (A) **SP1**, (B) **SP4**, (C) **SS1**, and (D) **SS4** with net NBO charges on the donor, acceptor, and π-conjugation path. The direction of dipoles is also shown and the change in dipole moments ($\Delta\mu$): (A) 5.913, (B) 14.26, (C) 18.31, and (D) 19.56 D. (Atom color codes: C = gray; H = white; N = blue; and O = red.)

Nuclear magnetic resonance spectra (^{1}H NMR and ^{13}C NMR) were recorded in CDCl$_3$ on a Bruker BioSpin Avance III HD at 500 MHz or a JEOL-FT NMR-AL at 400 MHz using TMS as an internal standard. High-resolution mass spectra (HRMS) were recorded on a Bruker LC−MS MICROTOF II spectrometer. Fourier transform infrared (FTIR) spectra were recorded in the range 650−4000 cm^{-1} on a Cary 630 FTIR (Agilent Technologies) spectrophotometer. Fluorescence measurements were performed on a Fluorolog Horiba fluorescence spectrometer, having a pulsed xenon flash lamp (50−60 Hz) and a 450 W CW ozone-free xenon arc lamp (250−2500 nm). The quantum yields were determined using an integrating sphere. Time-resolved fluorescence decay studies were performed on a PicoQuant FluoTime 300 high-performance fluorescence lifetime spectrometer. The instrument response function was recorded by using an aqueous solution of Ludox. UV−visible absorption data was recorded on a HITACHI U-2910 spectrophotometer using matched quartz cuvettes of 1 cm path length. The CV measurements were performed on an Autolab PGSTAT302N Metrohm workstation using a glass cell with a three-electrode assembly comprising a platinum counter electrode and a glassy carbon electrode as the working electrode. Ag/AgCl was used as the reference electrode. The thermal stability of the chromophores was determined by TGA using an STA7200 Hitachi thermal analysis system under a N$_2$ atmosphere at a heating rate of 20 °C min^{-1}.

4.2. Computational Details. Theoretical calculations were performed by using the Gaussian 09 suite of programs.[39] The molecular geometries of the chromophores were optimized at the DFT method employing the hybrid B3LYP functional group and the 6-31G (d,p) basis set according to the previous methods.[27] The first 25 excited states were used for TD-DFT calculations in gaseous medium and DCM as the solvent medium (CPCM) model. The molecular orbital contours were visualized using Gauss View 5.0.9. Using the

hyperpolarizability tensor components, β_{tot} values were calculated by using eqs 3 and 4

$$\beta_{tot} = [(\beta_{xxx} + \beta_{xyy} + \beta_{xzz})^2 + (\beta_{yyy} + \beta_{yzz} + \beta_{yxx})^2 + (\beta_{zzz} + \beta_{zxx} + \beta_{zyy})^2]^{1/2} \tag{3}$$

$$\beta_{tot} = (\beta_x^2 + \beta_y^2 + \beta_z^2)^{1/2} \tag{4}$$

4.3. Hyper-Rayleigh Scattering Measurements. The detailed HRS experimental setup is described elsewhere.[40] HRS experiments were conducted using a Q-switched Nd:YAG (Spectra-Physics, repetition rate 10 Hz and pulse width 10 ns) laser at a fundamental wavelength of 1064 nm. The complete details of the experiments are mentioned in the Supporting Information.

4.4. Synthesis and Characterization. Precursors 9,9-dimethylfluorene **2** and 9,9-dimethyl-2-nitrofluorene **3** were synthesized using previously reported methods.[27]

4.4.1. Synthesis of 2-Bromo-9,9-dimethyl-7-nitro-9H-fluorene (4). To a solution of **3** (4 g, 16.7 mmol) in acetic acid (20 mL) in a 100 mL three-necked flask, bromine (8 g, 50.1 mmol) was added dropwise for 2 h at 0 °C. The mixture was stirred at room temperature for 24 h. The solution was extracted with diethyl ether (3 × 30 mL), and the combined organic extract was sequentially washed with water and aqueous KOH solution. The organic extract was dried over anhydrous MgSO$_4$. Removal of the solvent furnished a light yellow product, which was purified by column chromatography using ethyl acetate/hexane (10:90, v/v) as eluents to isolate pure **4** as an orange solid (3.82 g, 82% yield). mp: 241−243 °C.[41] IR (ν_{max}, cm^{-1}): 670.9 (C−Br, str.) and 1513.3 (N═O, str.). ^{1}H NMR (400 MHz, CDCl$_3$, 25 °C): δ (ppm) 1.52 (s, 6H, 2 × CH$_3$), 7.52−7.54 (m, 1H, ArH), 7.61−7.62 (d, 1H, J = 2 Hz, ArH), 7.66 (dd, 1H, ArH), 7.79 (dd, J = 9 Hz, 1H, ArH), 8.24−8.27 (m, 2H, ArH). ^{13}C NMR (125 MHz, CDCl$_3$, 25 °C): δ (ppm) 26.7, 47.5, 118.4, 120.3, 122.7, 123.6, 123.7,

126.6, 130.9, 135.8, 144.6, 147.5, 154.3, 156.9. HRMS m/z: calcd for $C_{15}H_{12}BrNO_2$ $(M + H)^+$, 318.0129; found, 318.0130.

4.4.2. Synthesis of 9,9-Dimethyl-7-nitro-9H-fluorene-2-carbonitrile (5). To a solution of **4** (0.6 g, 1.89 mmol) in dry DMF (5 mL) in the microwave tube maintained under an inert atmosphere of dry N_2 gas, copper(I) cyanide (0.20 g, 2.23 mmol) was added. The reaction mixture was heated at 130 °C in a microwave reactor for 3.5 h, after which the solvent was removed under reduced pressure, and the residue was extracted with chloroform (3 × 20 mL). The combined chloroform extract was washed with water and dried over anhydrous $MgSO_4$. Removal of solvent yielded crude **5**, which was purified by column chromatography using ethyl acetate/hexane (15:85, v/v) as eluents to isolate pure **5** as a brownish-yellow solid (0.41 g, 81% yield). mp: 260−264 °C. IR (ν_{max}, cm^{-1}): 1513.3 (N=O, str.) and 2221.5 (C≡N, str.). ^1H NMR (500 MHz, $CDCl_3$, 25 °C): δ (ppm) 1.51 (s, 6H, 2 × CH_3), 7.65−7.66 (m, 1H, ArH), 7.71 (s, 1H, ArH), 7.82 (s, 1H, ArH), 7.84 (s, 1H, ArH), 8.24−8.26 (dd, J = 10 Hz, 1H, ArH), 8.27 (s, 1H, ArH). ^{13}C NMR (125 MHz, $CDCl_3$, 25 °C): δ (ppm) 26.5, 47.8, 112.4, 118.6, 118.9, 121.5, 122.1, 123.7, 126.8, 131.8, 141.2, 143.4, 148.3, 155.2, 155.4. HRMS m/z: calcd for $C_{16}H_{12}N_2O_2$ $(M + H)^+$, 265.0977; found, 265.0976.

4.4.3. Synthesis of 7-Amino-9,9-dimethyl-9H-fluorene-2-carbonitrile (6). In a round-bottomed flask, **5** (1 g, 3.79 mmol) and Pd/C (0.01 g 0.094 mmol) were added in absolute ethanol (125 mL), and the solution was warmed under an inert environment at 90 °C. Hydrazine hydrate (5 mL) was added at the same temperature, and the resulting mixture was refluxed for 2 h. After completion of the reaction (TLC), the solution was filtered over Celite, and the filtrate was concentrated under reduced pressure to obtain product **6**, which was purified by column chromatography. The product was obtained as a brown solid (0.62 g, 70% yield). mp: 295−297 °C. IR (ν_{max}, cm^{-1}): 1595.3 (N−H, bend) and 2221.5 (C≡N, str.). ^1H NMR (500 MHz, $CDCl_3$, 25 °C): δ (ppm) 1.36 (s, 6H, 2 × CH_3), 3.86 (s, 2H, NH), 6.59−6.61 (m, 1H, ArH), 6.66 (d, J = 2 Hz, 1H, ArH), 7.45 (d, J = 8.5 Hz, 1H, ArH), 7.47−7.54 (m, 3H, ArH). ^{13}C NMR (125 MHz, $CDCl_3$, 25 °C): δ (ppm) 26.2, 46.1, 107.2, 108.3, 113.7, 118.3, 119.5, 121.6, 125.3, 127.4, 130.9, 143.8, 147.2, 152.5, 155.9. HRMS m/z: calcd for $C_{16}H_{14}N_2$ $(M + H)^+$, 235.1157; found, 235.1131.

4.4.4. Synthesis of 7-(Dimethylamino)-9,9-dimethyl-9H-fluorene-2-carbonitrile (7). To a stirred mixture of **6** (0.50 g, 2.14 mmol) and paraformaldehyde (0.25 g, 8.3 mmol) in glacial acetic acid (10 mL), $NaBH_3CN$ (0.5 g, 7.9 mmol) was added in small portions at 0 °C. The mixture was allowed to warm to room temperature and stirred overnight before pouring into cold water (150 mL). The resultant mixture was extracted with ethyl acetate (3 × 30 mL). The combined organic extract was washed with saturated aqueous $NaHCO_3$ solution and dried with anhydrous Na_2SO_4. The solvent was removed under reduced pressure, and the residue was crystallized from ethanol to obtain **7** (0.46 g, 82% yield) as off-white crystals. mp: 267−269 °C. IR (ν_{max}, cm^{-1}): 1222.6 (C−N, str.), 1431.3 (CH_3, bend), 2221.5 (C≡N, str.). ^1H NMR (400 MHz, $CDCl_3$, 25 °C): δ (ppm) 1.47 (s, 6H, 2 × CH_3), 3.07 (s, 6H, 2 × NCH_3), 6.76 (m, 2H, ArH), 7.55−7.56 (m, 1H, ArH), 7.59−7.62 (m, 3H, ArH). ^{13}C NMR (100 MHz, $CDCl_3$, 25 °C): δ (ppm) 27.3, 40.9, 46.9, 106.3, 111.6, 118.6, 199.9, 120.7, 120.7, 122.2, 125.7, 126.8, 129.8, 138.9,

150.7, 154.9. HRMS m/z: calcd for $C_{18}H_{18}N_2$ $(M + H)^+$, 263.1548; found, 263.1544.

4.4.5. Synthesis of 7-(Dimethylamino)-9,9-dimethyl-9H-fluorene-2-carbaldehyde (8). DIBAL (0.054 g, 0.38 mmol, 30 mL, 1 M solution in heptane) was added to a solution of **7** (0.02 g, 0.076 mmol) in 5 mL of anhydrous DCM at 15 °C under an atmosphere of dry nitrogen gas. The mixture was stirred for 15 min, followed by reflux for 40 min. The reaction was cooled, and H_2SO_4 (1.0 M, 100 mL) was added slowly while keeping the temperature below 25 °C. After the addition of H_2SO_4 solution, the mixture was stirred for 1 h, and the DCM layer was separated. The aqueous layer was extracted with an additional 100 mL of DCM, and the combined organic extract was washed with 20% aqueous sodium bicarbonate solution and dried over anhydrous Na_2SO_4. Removal of solvent under reduced pressure yielded a bright green **8** (0.014 g, 70% yield). mp: 244−246 °C. IR (ν_{max}, cm^{-1}): 1222.6 (C−N, str.), 1431.3 (CH_3, bend), 1684.8 (C=O, str.), 2892.4 (CHO, str.) and 3056.4 (C−H, alkene). ^1H NMR (500 MHz, $CDCl_3$, 25 °C): δ (ppm) 1.42 (s, 6H, 2 × CH_3), 3.0 (s, 6H, 2 × NCH_3), 6.65−6.67 (m, 2H, ArH), 7.57−7.76 (m, 2H, ArH), 7.70−7.72 (m, 1H, ArH), 7.81 (br, 1H, ArH), 9.91 (s, 1H, CHO). ^{13}C NMR (125 MHz, $CDCl_3$, 25 °C): δ (ppm) 27.2, 40.7, 46.7, 105.8, 111.6, 118.4, 122.2, 122.4, 126.1, 131.1, 133.7, 146.7, 151.6, 153.4, 157.1, 192.1. HRMS m/z: calcd for $C_{18}H_{19}NO$ $(M + H)^+$, 266.1545; found, 266.1543.

4.4.6. Synthesis of 2-((7-(Dimethylamino)-9,9-dimethyl-9H-fluoren-2-yl)methylene)malononitrile (SS1). A solution of **8** (0.1 g, 0.38 mmol) and piperidine (0.09 g, 1.06 mmol) in anhydrous THF (15 mL) was cooled at 0 °C under an inert atmosphere; a solution of malononitrile (0.01 g, 0.15 mmol) in anhydrous THF (1 mL) was added dropwise, and the reaction was stirred at 0 °C. After completion (TLC), the reaction mixture was passed through Celite, and the bed was washed with DCM (20 mL). The combined filtrate was washed with water (2 × 20 mL), the DCM extract was dried over anhydrous Na_2SO_4, and the solvent was removed under reduced pressure to obtain crude **SS1**, which was purified by column chromatography using ethyl acetate/hexane (30:70, v/v) as eluents to isolate analytically pure red colored **SS1** (0.081 g, 69% yield). mp: 256−258 °C. IR (ν_{max}, cm^{-1}): 775.3 (C−H, alkene), 1222.6 (C−N, str.), 1431.3 (CH_3, bend), 1610 (C=C, str.) and 2221.5 (C≡N, str.). ^1H NMR (500 MHz, $CDCl_3$, 25 °C): δ (ppm) 1.52 (s, 6H, 2 × CH_3), 3.12 (s, 6H, 2 × NCH_3), 6.74−6.77 (m, 2H, ArH), 7.65−7.68 (m, 2H, ArH), 7.74 (s, 1H, ArH), 8.11 (m, 1H, ArH), 8.00 (s, 1H, CH). ^{13}C NMR (125 MHz, $CDCl_3$, 25 °C): δ (ppm) 27.1, 29.7, 40.6, 46.8, 105.5, 111.7, 113.9, 118.9, 122.7, 124.0, 125.6, 127.8, 132.1, 147.6, 152.0, 153.8, 157.6, 159.7. HRMS m/z: calcd for $C_{21}H_{19}N_3$ $(M + H)^+$, 314.1657; found, 314.1735.

4.4.7. Synthesis of (E)-2-(3-(2-(7-(Dimethylamino)-9,9-dimethyl-9H-fluoren-2-yl)vinyl)-5,5-dimethylcyclohex-2-en-1-ylidene)malononitrile (SS2). A solution of **8** (0.06 g, 0.23 mmol) and piperidine (0.008 g, 0.09 mmol) in anhydrous THF (10 mL) under an inert atmosphere was cooled at 0 °C; a solution of 2-(3,5,5-trimethyl-2-cyclohexylidene)malononitrile (0.03 g, 0.16 mmol) in anhydrous THF (3 mL) was added dropwise, and the reaction was stirred at 0 °C. After evaporating THF, the reaction mixture was extracted with organic solvent and water. The organic solvent dried over anhydrous Na_2SO_4, and the solvent was removed under reduced pressure to obtain a crude product, which was further purified by column chromatography using 15:85 (ethyl

acetate/hexane, v/v) to isolate a dark maroon solid **SS2** (0.076 g, 78% yield). mp: 298−302 °C. IR (ν_{max}, cm^{-1}): 775.3 (C−H, alkene), 1222.6 (C−N, str.), 1431.3 (CH$_3$, bend), 1610 (C=C, str.) and 2221.5 (C≡N, str.). ^{1}H NMR (500 MHz, CDCl$_3$, 25 °C): δ (ppm) 1.12 (s, 6H, 2 × CH$_3$), 1.52 (s, 6H, 2 × CH$_3$), 2.52 (s, 2H, CH$_2$), 2.64 (s, 2H, CH$_2$), 3.09 (s, 6H, 2 × NCH$_3$), 6.74−6.67 (m, 1H, ArH), 6.78 (m, 1H, ArH), 6.88 (s, 1H, Ar), 7.04−7.07 (m, 1H, CH), 7.16−7.19 (m, 1H, CH), 7.44−7.45 (m, 1H, ArH), 7.58 (s, 1H, ArH), 7.59−7.63 (m, 2H, Ar). ^{13}C NMR (125 MHz, CDCl$_3$, 25 °C): δ (ppm) 21.0, 27.5, 28.1, 32.0, 39.2, 40.8, 46.7, 66.9, 67.9, 106.1, 111.5, 113.1, 118.9, 120.9, 121.4, 122.8, 127.2, 127.9, 132.6, 138.3, 142.4, 151.1, 153.7, 154.6, 156.2, 169.3, 170.4. HRMS m/z: calcd for C$_{30}$H$_{31}$N$_3$ (M + H)$^+$, 434.2596; found, 434.2595.

4.4.8. Synthesis of (E)-2-(4-Bromophenyl)-3-(7-(dimethylamino)-9,9-dimethyl-9H-fluoren-2-yl)acrylonitrile (SS3). To a solution of **8** (0.1 g, 0.38 mmol) and 4-bromophenylacetonitrile (0.08 g, 0.41 mmol) in dry methanol (5 mL), a solution of potassium hydroxide (1.5 mL, 0.6 M) was added dropwise under vigorous stirring. Upon completion of the addition, the mixture turned cloudy, and the suspension was stirred for 24 h at room temperature and subsequently cooled, which resulted in the precipitation of the product which was filtered and recrystallized from ethanol to obtain pure **SS3** as a yellow solid (0.13 g, 78% yield). mp: 240−242 °C. IR (ν_{max}, cm^{-1}): 641.1 (C−Br, str.), 775.3 (C−H, C=C), 1222.6 (C−N, str.), 1431.3 (CH$_3$, bend), 1610 (C=C, str.) and 2221.5 (C≡N, str.). ^{1}H NMR (500 MHz, CDCl$_3$, 25 °C): δ (ppm) 1.54 (s, 6H, 2 × CH$_3$), 3.09 (s, 6H, 2 × NCH$_3$), 6.75−6.77 (m, 1H, ArH), 6.79 (m, 1H, ArH), 7.57−7.61 (m, 5H, ArH), 7.64−7.66 (m, 2H, ArH), 7.81−7.83 (m, 1H, ArH), 8.03 (s, 1H, CH). ^{13}C NMR (125 MHz, CDCl$_3$, 25 °C): δ (ppm) 23.2, 27.2, 29.7, 40.7, 46.9, 105.7, 107.3, 111.6, 117.3, 118.7, 120.3, 121.9, 122.1, 125.8, 128.8, 129.6, 131.5, 132.3, 144.7, 151.6, 153.2, 156.2. HRMS m/z: calcd for C$_{26}$H$_{23}$BrN$_2$ (M + H)$^+$, 443.1123; found, 443.1120.

4.4.9. Synthesis of (E)-3-(7-(Dimethylamino)-9,9-dimethyl-9H-fluoren-2-yl)-2-(4-nitrophenyl)acrylonitrile (SS4). To a solution of **8** (0.2 g, 0.75 mmol) and 4-nitrophenylacetonitrile (0.184 g, 1.13 mmol) in dry methanol (5 mL), a solution of potassium hydroxide (2 mL, 0.6 M) was added dropwise under vigorous stirring. Upon completion of the addition, the suspension was stirred for 10 h at room temperature and resulted in the precipitation of the product which was filtered and recrystallized from ethanol to obtain analytically pure **SS4** as a dark red solid (0.23 g, 74% yield). mp: 280−282 °C. IR (ν_{max}, cm^{-1}): 775.3 (C−H, alkene), 1222.6 (C−N, str.), 1431.3 (CH$_3$, bend), 1513.3 (N=O, str.), 1610 (C=C, str.) and 2221.5 (C≡N, str.). ^{1}H NMR (500 MHz, CDCl$_3$, 25 °C): δ (ppm) 1.53 (s, 6H, 2 × CH$_3$), 3.08 (s, 6H, 2 × NCH$_3$), 6.73−6.76 (m, 2H, ArH), 7.63−7.66 (m, 2H, ArH), 7.72 (s, 1H, ArH), 7.84−7.86 (m, 3H, ArH), 8.07 (s, 1H, CH), 8.08 (s, 1H, ArH), 8.30−8.31 (m, 1H, Ar). ^{13}C NMR (125 MHz, CDCl$_3$, 25 °C): δ (ppm) 27.3, 40.7, 46.8, 105.9, 105.9, 111.6, 118.1, 118.8, 121.9, 123.4, 124.3, 126.3, 126.5, 129.7, 130.2, 130.4, 141.5, 144.3, 146.2, 147.4, 151.5, 153.5, 156.8. HRMS m/z: calcd for C$_{26}$H$_{23}$N$_3$O$_2$ (M + H)$^+$, 410.1869; found, 410.1867.

4.4.10. Synthesis of (E)-4-(1-Cyano-2-(7-(dimethylamino)-9,9-dimethyl-9H-fluoren-2-yl)vinyl)benzonitrile (SS5). A solution of compound **SS3** (0.5 g, 1.13 mmol) in dry DMF (7 mL) was maintained under an inert atmosphere, and copper(I) cyanide (0.252 g, 2.81 mmol) was added in the microwave

tube. The reaction mixture was heated at 130 °C in a microwave reactor for 4 h, after which the solvent was removed under reduced pressure, and the compound was extracted with (3 × 20 mL). The combined layer was extracted with water, and the organic extract was dried over anhydrous Na$_2$SO$_4$. Removal of solvent yielded crude **SS5** as a pure orange solid (0.28 g, 64% yield). mp: 254−256 °C. IR (ν_{max}, cm^{-1}): 775.3 (C−H, alkene), 1222.6 (C−N, str.), 1431.3 (CH$_3$, bend), 1610 (C=C, str.) and 2221.5 (C≡N, str.). ^{1}H NMR (500 MHz, CDCl$_3$, 25 °C): δ (ppm) 1.52 (s, 6H, 2 × CH$_3$), 3.08 (s, 6H, 2 × NCH$_3$), 6.72−6.73 (m, 1H, ArH), 6.74−6.76 (m, 1H, ArH), 7.62−7.66 (m, 3H, ArH), 7.72−7.74 (m, 2H, ArH), 7.78−7.80 (m, 2H, ArH), 7.81−7.83 (m, 1H, ArH), 8.05 (s, 1H, CH). ^{13}C NMR (125 MHz, CDCl$_3$, 25 °C): δ (ppm) 27.3, 40.7, 46.8, 105.9, 106.3, 111.5, 111.8, 118.1, 118.5, 118.8, 121.8, 123.3, 126.2, 126.5, 129.7, 130.2, 132.7, 139.6, 144.1, 146.6, 151.4, 153.5, 156.7. HRMS m/z: calcd for C$_{27}$H$_{23}$N$_3$ (M + H)$^+$, 390.1970; found, 390.1971.

■ ASSOCIATED CONTENT

ⓢ Supporting Information

The Supporting Information is available free of charge at https://pubs.acs.org/doi/10.1021/acsomega.2c04795.

> HRS measurements, spectral data (^{1}H and ^{13}C NMR, FTIR, and HRMS), single crystal X-ray crystallographic data, density functional theory (DFT) calculation data, photophysical (UV−visible absorption, fluorescence emission) spectra and tables, quantum yields, time correlated single photon counting (TCSPC) data, thermogravimetric analysis (TGA) curves, NBO calculation data, HRS curves and procedure for MPF correction, quadratic curves, electrostatic potential maps, Cartesian coordinates etc. (PDF)

■ AUTHOR INFORMATION

Corresponding Authors

Paramjit Kaur − *Department of Chemistry, UGC Centre of Advanced Study, Guru Nanak Dev University, Amritsar 143005, India*; Email: paramjit19in@yahoo.co.in

Kamaljit Singh − *Department of Chemistry, UGC Centre of Advanced Study, Guru Nanak Dev University, Amritsar 143005, India;* ⓞ orcid.org/0000-0002-9752-3363; Email: kamaljit.chem@gndu.ac.in

Authors

Shivani − *Department of Chemistry, UGC Centre of Advanced Study, Guru Nanak Dev University, Amritsar 143005, India*

Akriti Mishra − *Department of Inorganic and Physical Chemistry, Indian Institute of Science, Bangalore 560012, India*

Complete contact information is available at:
https://pubs.acs.org/10.1021/acsomega.2c04795

Author Contributions

K.S. planned the work and designed the chromophores, planned the synthetic strategy, and prepared the manuscript draft. P.K. assisted in interpreting the photophysical and other data as well as drafting the manuscript. S. performed the synthesis, including characterization and photophysical studies, and DFT calculations and compiled the experimental part. She also performed HRS measurements along with A.M. The manuscript draft was approved by all the authors.

Notes

The authors declare no competing financial interest.

REFERENCES

(1) Zhang, S.-Y.; Shu, X.; Zeng, Y.; Liu, Q.-Y.; Du, Z.-Y.; He, C.-T.; Zhang, W.-X.; Chen, X.-M. Molecule-Based Nonlinear Optical Switch with Highly Tunable On-Off Temperature Using a Dual Solid Solution Approach. *Nat. Commun.* **2020**, *11*, 2752.

(2) Hänsel, M.; Barta, C.; Rietze, C.; Utecht, M.; Rueck-Braun, K.; Saalfrank, P.; Tegeder, P. 2-Dimensional Nonlinear Optical Switching Materials: Molecular Engineering towards High Nonlinear Optical Contrasts. *J. Phys. Chem. C* **2018**, *122*, 25555−25564.

(3) Boixel, J.; Guerchais, V.; Le Bozec, H. L.; Jacquemin, D.; Amar, A.; Boucekkine, A.; Colombo, A.; Dragonetti, C.; Marinotto, D.; Roberto, D.; Righetto, S.; De Angelis, R. D. Second-Order NLO Switches from Molecules to Polymer Films Based on Photochromic Cyclometalated Platinum (II) Complexes. *J. Am. Chem. Soc.* **2014**, *136*, 5367−5375.

(4) Saravanakumar, M.; Chandrasekaran, J.; Krishnakumar, M.; Babu, B.; Vinitha, G.; Anis, M. Experimental and Quantum Chemical Studies on SHG, Z-scan and Optical Limiting Investigation of 2-Amino-5-Bromopyridinium Trifluoroacetate Single Crystal for Opto-electronic Applications. *J. Phys. Chem. Solids* **2020**, *136*, 109133.

(5) Zhang, C.; Li, X.; Wang, Y.; An, M.; Sun, Z. A Hydrazone Organic Optical Modulator with a π Electronic System for Ultrafast Photonics. *J. Mater. Chem. C* **2021**, *9*, 11306−11313.

(6) Zhang, Y.; He, J.; Saris, P. J. G.; Chae, H. U.; Das, S.; Kapadia, R.; Armani, A. M. Multifunctional Photoresponsive Organic Molecule for Electric Field Sensing and Modulation. *J. Mater. Chem. C* **2022**, *10*, 1204−1211.

(7) Zhang, Z.; Wang, Z.; Shi, T.; Bi, C.; Rao, F.; Cai, Y.; Liu, Q.; Wu, H.; Zhou, P. Memory Materials and Devices: From Concept to Application. *InfoMat* **2020**, *2*, 261−290.

(8) Wu, J.; Li, Z.; Luo, J.; Jen, A. K.-Y. High-Performance Organic Second- and Third-Order Nonlinear Optical Materials for Ultrafast Information Processing. *J. Mater. Chem. C* **2020**, *8*, 15009−15026.

(9) Semin, S.; Li, X.; Duan, Y.; Rasing, T. Nonlinear Optical Properties and Applications of Fluorenone Molecular Materials. *Adv. Opt. Mater.* **2021**, *9*, 2100327.

(10) Xie, Z.; Lefier, Y.; Suarez, M. A.; Mivelle, M.; Salut, R.; Merolla, J.-M.; Grosjean, T. Doubly Resonant Photonic Antenna for Single Infrared Quantum Dot Imaging at Telecommunication Wavelengths. *Nano Lett.* **2017**, *17*, 2152−2158.

(11) Cleuvenbergen, S. V.; Asselberghs, I.; Vanormelingen, W.; Verbiest, T.; Franz, E.; Clays, K.; Kuzyk, M. G.; Koeckelberghs, G. Record-High Hyperpolarizabilities in Conjugated Polymers. *J. Mater. Chem. C* **2014**, *2*, 4533−4538.

(12) Kaur, S.; Kaur, M.; Kaur, P.; Clays, K.; Singh, K. Ferrocene Chromophores Continue to Inspire. Fine-Tuning and Switching of the Second-Order Nonlinear Optical Response. *Coord. Chem. Rev.* **2017**, *343*, 185−219.

(13) Ye, J.-T.; Liu, J.-H.; Zhang, Q.; Qiu, Y.-Q.; Wang, L.-H. Tuning of Second-Order Nonlinear Optical Properties Based on [2.2] Paracyclophanes Isomer: The Relative Configuration and Polarizable Environment. *J. Phys. Chem. C* **2020**, *124*, 21692−21701.

(14) In, Y. R.; Han, J. M.; Kwon, J. E.; Kim, B.-G.; Moon, H. C. Rational Molecular Design of Electrochromic Conjugated Polymers: Toward High-Performance Systems with Ultrahigh Coloration Efficiency. *Chem. Eng. J.* **2022**, *433*, 133808.

(15) Xu, J.; Semin, S.; Rasing, T.; Rowan, A. E. Organized Chromophoric Assemblies for Nonlinear Optical Materials: Towards (Sub) Wavelength Scale Architectures. *Small* **2015**, *11*, 1113−1129.

(16) Valdivia-Berroeta, G. A.; Jackson, E. W.; Kenney, K. C.; Wayment, A. X.; Tangen, I. C.; Bahr, C. B.; Smith, S. J.; Michaelis, D. J.; Johnson, J. A. Designing Non-Centrosymmetric Molecular Crystals: Optimal Packing May Be Just One Carbon Away. *Adv. Funct. Mater.* **2020**, *30*, 1904786.

(17) Balakrishna, K.; Sampath, R.; Vishwam, T.; Samui, A. B.; Joshi, M. P.; Mohan, S. R. Synthesis and Characterization of Carbazole Based Donor-Acceptor-Donor Type Polymer for NLO Applications. *J. Phys.: Conf. Ser.* **2020**, *1495*, 012026.

(18) Li, Y.-Y.; Wang, J.-Q.; Liu, P.-F.; Lin, H.; Chen, L.; Wu, L.-M. Centrosymmetric to Noncentrosymmetric Structural Transformation of New Quaternary Selenides Induced by Isolated Dimeric $[Sn_2Se_4]$ Units: from $Ba_8Ga_2Sn_7Se_{18}$ to $Ba_{10}Ga_2Sn_9Se_{22}$. *RSC Adv.* **2017**, *7*, 8082−8089.

(19) Nagai, Y.; Ishiba, K.; Yamamoto, R.; Yamada, T.; Morikawa, M.; Kimizuka, N. Light-Triggered, Non-Centrosymmetric Self-Assembly of Aqueous Arylazopyrazoles at the Air-Water Interface and Switching of Second-Harmonic Generation. *Angew. Chem., Int. Ed.* **2021**, *60*, 6333−6338.

(20) Gopalakrishnan, M.; Viswanathan, T.; David, E.; Thirumoorthy, K.; Bhuvanesh, N. S. P.; Palanisami, N. Second-Order Nonlinear Optical Properties of Eight-Membered Centrosymmetric Cyclic Borasiloxanes. *New J. Chem.* **2019**, *43*, 10948−10958.

(21) Bodedla, G. B.; Justin Thomas, K. R. J.; Fan, M.-S.; Ho, K.-C. Benzimidazole-Branched Isomeric Dyes: Effect of Molecular Constitution on Photophysical, Electrochemical, and Photovoltaic Properties. *J. Org. Chem.* **2016**, *81*, 640−653.

(22) Tan, L.-L.; Huang, J.-F.; Shen, Y.; Xiao, L.-M.; Liu, J.-M.; Kuang, D.-B.; Su, C.-Y. Highly Efficient and Stable Organic Sensitizers with Duplex Starburst Triphenylamine and Carbazole Donors for Liquid and Quasi-Solid-State Dye-Sensitized Solar Cell. *J. Mater. Chem. A* **2014**, *2*, 8988−8994.

(23) Kaur, P.; Singh, K. Second-Order Nonlinear Polarizability of "Push-Pull" Chromophores. A Decade of Progress in Donor-π-Acceptor Materials. *Chem. Rec.* **2022**, *22*, No. e202200024.

(24) Khalid, M.; Lodhi, H. M.; Khan, M. U.; Imran, M. Structural Parameter-Modulated Nonlinear Optical Amplitude of Acceptor-π-D-π-Donor-Configured Pyrene Derivatives: a DFT Approach. *RSC Adv.* **2021**, *11*, 14237−14250.

(25) Kaur, S.; Van Steerteghem, N. V.; Kaur, P.; Clays, K.; Singh, K. Synthesis, Characterization and Second-Order Nonlinear Optical Behaviour of Ferrocene-Diketopyrrolopyrrole Dyads: The Effect of Alkene *vs.* Alkyne Linkers. *J. Mater. Chem. C* **2016**, *4*, 9717−9726.

(26) Ye, J.-T.; Wang, L.; Wang, H.-Q.; Pan, X.-M.; Xie, H.; Qiu, Y. Effective Impact of Dielectric Constant on Thermally Activated Delayed Fluorescence and Nonlinear Optical Properties: Through-Bond/-Space Charge Transfer Architectures. *J. Phys. Chem. C* **2018**, *122*, 18850−18859.

(27) Shivani; Mishra, A.; Kumar, V.; Kaur, P.; Singh, K. Synthesis, Linear and Non-linear Optical Properties of "Push-Pull" Chromophores Based on 9,9-Dimethyl-9H-Fluoren-2-Amine. *Dyes Pigm.* **2022**, *200*, 110160.

(28) Adeniyi, A. A.; Ngake, L. T.; Conradie, J. Cyclic Voltammetric Study of 2-hydroxybenzophenone (HBP) Derivatives and the Correspondent Change in the Orbital Energy Levels in Different Solvents. *Electroanalysis* **2020**, *32*, 2659−2668.

(29) Hrobárik, P.; Sigmundová, I.; Zahradník, P.; Kasák, P.; Arion, V.; Franz, E.; Clays, K. Molecular Engineering of Benzothiazolium Salts with Large Quadratic Hyperpolarizabilities: Can Auxiliary Electron-Withdrawing Groups Enhance Nonlinear Optical Responses? *J. Phys. Chem. C* **2010**, *114*, 22289−22302.

(30) Al-Ansari, I. A. Z. Role of Solvent Polarity and Hydrogen Bonding on Excited-State Fluorescence of 3-[(E)-{4-(N,N-Dimethylamino-Benzylidene}-Amino)-2-Naphthoic Acid (DMAMN): Isomerization Versus Rotomerization. *J. Phys. Chem. A* **2018**, *122*, 1838−1854.

(31) Guo, X.; Wang, S.; Xia, A.; Su, H. Determination of the Formation of Dark State via Depleted Spontaneous Emission in a Complex Solvated Molecule. *J. Phys. Chem. A* **2007**, *111*, 5800−5805.

(32) Kumar, S. Comparative Study of Excited State Dipole Moment of Coumarin Laser Dyes: Solvent and Substituent Effect. *J. Mater. Sci. Eng. B* **2014**, *4*, 358−365.

(33) Sayresmith, N.; Saminathan, A.; Sailer, J. K.; Patberg, S. M.; Sandor, K.; Krishnan, Y.; Walter, M. G. Photostable Voltage Sensitive Dyes Based on Simple, Solvatofluorochromic, Asymmetric Thiazolo-thiazoles. *J. Am. Chem. Soc.* **2019**, *141*, 18780−18790.

(34) Lakowicz, J. R. *Principles of Fluorescence Spectroscopy*, 3rd ed.; Springer: Berlin, 2006.

(35) Hapiot, P.; Lagrost, C.; Le Floch, F. L.; Raoult, E.; Rault-Berthelot, J. Comparative Study of the Oxidation of Fluorene and 9,9-Disubstituted Fluorenes and Their Related 2,7′-Dimers and Trimer. *Chem. Mater.* **2005**, *17*, 2003−2012.

(36) Oudar, J. L.; Chemla, D. S. Hyperpolarizabilities of the Nitroanilines and Their Relations to the Excited State Dipole Moment. *J. Chem. Phys.* **1977**, *66*, 2664.

(37) Pérez-Moreno, J.; Zhao, Y.; Clays, K.; Kuzyk, M. G.; Shen, Y.; Qiu, L.; Hao, J.; Guo, K. Modulated Conjugation as a Means of Improving the Intrinsic Hyperpolarizability. *J. Am. Chem. Soc.* **2009**, *131*, 5084−5093.

(38) Watkins, D. S.; Kuzyk, M. G. The Effect of Electron Interactions on the Universal Properties of Systems with Optimized Off-Resonant Intrinsic Hyperpolarizability. *J. Chem. Phys.* **2011**, *134*, 094109.

(39) Frisch, M. J.; Trucks, G. W.; Schlegel, H. B.; Scuseria, G. E.; Robb, M. A.; Cheeseman, J. R.; Scalmani, G.; Barone, V.; Mennucci, B.; Petersson, G. A.; et al. *Gaussian 09*, Revision B.01; Gaussian, Inc.: Wallingford CT, 2010.

(40) Clays, K.; Coe, B. J. Design Strategies versus Limiting Theory for Engineering Large Second-Order Nonlinear Optical Polar-izabilities in Charged Organic Molecules. *Chem. Mater.* **2003**, *15*, 642−648.

(41) Hosseinzadeh, R.; Mohadjerani, M.; Pooryousef, M.; Eslami, A.; Emami, S. A New Boronic Acid Fluorescent Sensor Based on Fluorene for Monosaccharides at Physiological pH. *Spectrochim. Acta, Part A* **2015**, *144*, 53−60.